Search for the neutral Higgs bosons of the Standard Model and the MSSM in e^+e^- collisions at $\sqrt{s} = 189\,\text{GeV}$

The ALEPH Collaboration

R. Barate, D. Decamp, P. Ghez, C. Goy, S. Jezequel, J.-P. Lees, F. Martin, E. Merle, M.-N. Minard, B. Pietrzyk
Laboratoire de Physique des Particules (LAPP), IN[2]P[3]-CNRS, 74019 Annecy-le-Vieux Cedex, France

R. Alemany, S. Bravo, M.P. Casado, M. Chmeissani, J.M. Crespo, E. Fernandez, M. Fernandez-Bosman, Ll. Garrido[15], E. Graugés, A. Juste, M. Martinez, G. Merino, R. Miquel, Ll.M. Mir, P. Morawitz, A. Pacheco, I. Riu, H. Ruiz
Institut de Física d'Altes Energies, Universitat Autònoma de Barcelona, 08193 Bellaterra (Barcelona), Spain[7]

A. Colaleo, D. Creanza, M. de Palma, G. Iaselli, G. Maggi, M. Maggi, S. Nuzzo, A. Ranieri, G. Raso, F. Ruggieri, G. Selvaggi, L. Silvestris, P. Tempesta, A. Tricomi[3], G. Zito
Dipartimento di Fisica, INFN Sezione di Bari, 70126 Bari, Italy

X. Huang, J. Lin, Q. Ouyang, T. Wang, Y. Xie, R. Xu, S. Xue, J. Zhang, L. Zhang, W. Zhao
Institute of High Energy Physics, Academia Sinica, Beijing, P.R. China[8]

D. Abbaneo, G. Boix[6], O. Buchmüller, M. Cattaneo, F. Cerutti, G. Davies, G. Dissertori, H. Drevermann, R.W. Forty, M. Frank, F. Gianotti, T.C. Greening, A.W. Halley, J.B. Hansen, J. Harvey, P. Janot, B. Jost, M. Kado, O. Leroy, P. Maley, P. Mato, A. Minten, A. Moutoussi, F. Ranjard, L. Rolandi, D. Schlatter, M. Schmitt[20], O. Schneider[2], P. Spagnolo, W. Tejessy, F. Teubert, E. Tournefier, A. Valassi, J.J. Ward, A.E. Wright
European Laboratory for Particle Physics (CERN), 1211 Geneva 23, Switzerland

Z. Ajaltouni, F. Badaud, G. Chazelle, O. Deschamps, S. Dessagne, A. Falvard, C. Ferdi, P. Gay, C. Guicheney, P. Henrard, J. Jousset, B. Michel, S. Monteil, J-C. Montret, D. Pallin, J.M. Pascolo, P. Perret, F. Podlyski
Laboratoire de Physique Corpusculaire, Université Blaise Pascal, IN[2]P[3]-CNRS, Clermont-Ferrand, 63177 Aubière, France

J.D. Hansen, J.R. Hansen, P.H. Hansen[1], B.S. Nilsson, A. Wäänänen
Niels Bohr Institute, 2100 Copenhagen, Denmark[9]

G. Daskalakis, A. Kyriakis, C. Markou, E. Simopoulou, A. Vayaki
Nuclear Research Center Demokritos (NRCD), 15310 Attiki, Greece

A. Blondel[23], J.-C. Brient, F. Machefert, A. Rougé, M. Swynghedauw, R. Tanaka, H. Videau
Laboratoire de Physique Nucléaire et des Hautes Energies, Ecole Polytechnique, IN[2]P[3]-CNRS, 91128 Palaiseau Cedex, France

E. Focardi, G. Parrini, K. Zachariadou
Dipartimento di Fisica, Università di Firenze, INFN Sezione di Firenze, 50125 Firenze, Italy

A. Antonelli, G. Bencivenni, G. Bologna[4], F. Bossi, P. Campana, G. Capon, V. Chiarella, P. Laurelli, G. Mannocchi[1,5], F. Murtas, G.P. Murtas, L. Passalacqua, M. Pepe-Altarelli
Laboratori Nazionali dell'INFN (LNF-INFN), 00044 Frascati, Italy

M. Chalmers, J. Kennedy, J.G. Lynch, P. Negus, V. O'Shea, B. Raeven, D. Smith, P. Teixeira-Dias, A.S. Thompson
Department of Physics and Astronomy, University of Glasgow, Glasgow G12 8QQ, UK[10]

R. Cavanaugh, S. Dhamotharan, C. Geweniger[1], P. Hanke, V. Hepp, E.E. Kluge, G. Leibenguth, A. Putzer, K. Tittel, S. Werner[19], M. Wunsch[19]
Kirchhoff-Institut für Physik, Universität Heidelberg, 69120 Heidelberg, Germany[16]

R. Beuselinck, D.M. Binnie, W. Cameron, P.J. Dornan, M. Girone, S. Goodsir, N. Marinelli, E.B. Martin, J. Nash,
J. Nowell, H. Przysieezniak[1], A. Sciabà, J.K. Sedgbeer, J.C. Thompson[14], E. Thomson, M.D. Williams
Department of Physics, Imperial College, London SW7 2BZ, UK[10]

V.M. Ghete, P. Girtler, E. Kneringer, D. Kuhn, G. Rudolph
Institut für Experimentalphysik, Universität Innsbruck, 6020 Innsbruck, Austria[18]

C.K. Bowdery, P.G. Buck, D.P. Clarke, G. Ellis, A.J. Finch, F. Foster, G. Hughes, R.W.L. Jones, N.A. Robertson,
M. Smizanska
Department of Physics, University of Lancaster, Lancaster LA1 4YB, UK[10]

I. Giehl, F. Hölldorfer, K. Jakobs, K. Kleinknecht, M. Kröcker, A.-S. Müller, H.-A. Nürnberger, G. Quast, B. Renk,
E. Rohne, H.-G. Sander, S. Schmeling, H. Wachsmuth C. Zeitnitz, T. Ziegler
Institut für Physik, Universität Mainz, 55099 Mainz, Germany[16]

A. Bonissent, J. Carr, P. Coyle, A. Ealet, D. Fouchez, P. Payre, D. Rousseau, A. Tilquin
Centre de Physique des Particules, Faculté des Sciences de Luminy, IN^{2}P^3-CNRS, 13288 Marseille, France

M. Aleppo, M. Antonelli, S. Gilardoni, F. Ragusa
Dipartimento di Fisica, Università di Milano e INFN Sezione di Milano, 20133 Milano, Italy

V. Büscher, H. Dietl, G. Ganis, K. Hüttmann, G. Lütjens, C. Mannert, W. Männer, H.-G. Moser, S. Schael,
R. Settles[1], H. Seywerd, H. Stenzel, W. Wiedenmann, G. Wolf
Max-Planck-Institut für Physik, Werner-Heisenberg-Institut, 80805 München, Germany[16]

P. Azzurri, J. Boucrot[1], O. Callot, S. Chen, M. Davier, L. Duflot, J.-F. Grivaz, Ph. Heusse, A. Jacholkowska[1],
J. Lefrançois, L. Serin, J.-J. Veillet, I. Videau[1], J.-B. de Vivie de Régie, D. Zerwas
Laboratoire de l'Accélérateur Linéaire, Université de Paris-Sud, IN^{2}P^3-CNRS, 91898 Orsay Cedex, France

G. Bagliesi, T. Boccali, C. Bozzi[12], G. Calderini, V. Ciulli, R. Dell'Orso, I. Ferrante, A. Giassi, A. Gregorio,
F. Ligabue, P.S. Marrocchesi, A. Messineo, F. Palla, G. Rizzo, G. Sanguinetti, G. Sguazzoni, R. Tenchini[1], A. Venturi,
P.G. Verdini
Dipartimento di Fisica dell'Università, INFN Sezione di Pisa, e Scuola Normale Superiore, 56010 Pisa, Italy

G.A. Blair, J. Coles, G. Cowan, M.G. Green, D.E. Hutchcroft, L.T. Jones, T. Medcalf, J.A. Strong
Department of Physics, Royal Holloway & Bedford New College, University of London, Surrey TW20 OEX, UK[10]

R.W. Clifft, T.R. Edgecock, P.R. Norton, I.R. Tomalin
Particle Physics Dept., Rutherford Appleton Laboratory, Chilton, Didcot, Oxon OX11 OQX, UK[10]

B. Bloch-Devaux, P. Colas, B. Fabbro, G. Faïf, E. Lançon, M.-C. Lemaire, E. Locci, P. Perez, J. Rander,
J.-F. Renardy, A. Rosowsky, P. Seager[13], A. Trabelsi[21], B. Tuchming, B. Vallage
CEA, DAPNIA/Service de Physique des Particules, CE-Saclay, 91191 Gif-sur-Yvette Cedex, France[17]

S.N. Black, J.H. Dann, C. Loomis, H.Y. Kim, N. Konstantinidis, A.M. Litke, M.A. McNeil, G. Taylor
Institute for Particle Physics, University of California at Santa Cruz, Santa Cruz, CA 95064, USA[22]

C.N. Booth, S. Cartwright, F. Combley, P.N. Hodgson, M. Lehto, L.F. Thompson
Department of Physics, University of Sheffield, Sheffield S3 7RH, UK[10]

K. Affholderbach, A. Böhrer, S. Brandt, C. Grupen, J. Hess, A. Misiejuk, G. Prange, U. Sieler
Fachbereich Physik, Universität Siegen, 57068 Siegen, Germany[16]

C. Borean, G. Giannini, B. Gobbo
Dipartimento di Fisica, Università di Trieste e INFN Sezione di Trieste, 34127 Trieste, Italy

J. Putz, J. Rothberg, S. Wasserbaech, R.W. Williams
Experimental Elementary Particle Physics, University of Washington, WA 98195 Seattle, USA

S.R. Armstrong, P. Elmer, D.P.S. Ferguson, Y. Gao, S. González, O.J. Hayes, H. Hu, S. Jin, J. Kile, P.A. McNamara
III, J. Nielsen, W. Orejudos, Y.B. Pan, Y. Saadi, I.J. Scott, J. Walsh, J.H. von Wimmersperg-Toeller, Sau Lan Wu,
X. Wu, G. Zobernig
Department of Physics, University of Wisconsin, Madison, WI 53706, USA[11]

Abstract. Neutral Higgs bosons of the Standard Model and of the MSSM are searched for in the data collected at a centre-of-mass energy of 188.6 GeV by the ALEPH experiment at LEP, with an integrated luminosity of 176 pb^{-1}. No evidence for a signal is found. A lower limit of 92.9 GeV/c^2 at 95% confidence level is set on the mass of the Standard Model Higgs boson, with an expected sensitivity of 95.9 GeV/c^2. In the MSSM, for $\tan\beta \geq 0.7$ and for benchmark parameter choices, observed (expected) lower limits of 82.5 (83.1) GeV/c^2 and 82.6 (83.2) GeV/c^2 are derived for the masses of the neutral Higgs bosons h and A, respectively. An update of the general MSSM parameter scan is also presented.

1 Introduction

At LEP2, Standard Model Higgs boson production is dominated by the Higgsstrahlung process, e$^+$e$^-\rightarrow$HZ, with smaller contributions from the WW- and ZZ-fusion processes to the H$\nu\bar{\nu}$ and He$^+$e$^-$ final states. In the framework of the Minimal Supersymmetric Standard Model (MSSM) neutral Higgs bosons are produced via two complementary reactions: the Higgsstrahlung process e$^+$e$^-\rightarrow$ hZ and the associated pair production e$^+$e$^-\rightarrow$hA. The cross section of the Higgsstrahlung process is proportional to $\sin^2(\beta-\alpha)$, where $\tan\beta$ is the ratio of the vacuum ex-

pectation values of the two Higgs doublets and α is the mixing angle in the CP-even Higgs sector. The hA cross section is proportional to $\cos^2(\beta-\alpha)$. In the mass range of interest for LEP2 searches, the main H decay channel is H$\rightarrow$b$\bar{\text{b}}$; the $\tau^+\tau^-$ decay mode is also relevant. The same decay modes are dominant for h and A when $\tan\beta > 1$. The searches described in this paper cover most of the topologies arising from the HZ process, with H$\rightarrow$b$\bar{\text{b}}$ or $\tau^+\tau^-$and Z$\rightarrow$e$^+$e$^-$, $\mu^+\mu^-$, $\tau^+\tau^-$, $\nu\bar{\nu}$ or q$\bar{\text{q}}$, and also from the hA process, with h and A decaying to b$\bar{\text{b}}$ or $\tau^+\tau^-$. In the following, h denotes both the Standard Model Higgs boson and the lighter CP-even neutral Higgs boson of the MSSM.

Searches for neutral Higgs bosons have already been performed by ALEPH up to a centre-of-mass energy of 184 GeV. No evidence for a signal was found and a lower limit of 87.9 GeV/c^2 was set at the 95% confidence level (CL) on the Standard Model Higgs boson mass [1,2]. In the MSSM, masses of h and A lower than 72.2 GeV/c^2 and 76.1 GeV/c^2 respectively were excluded at the 95% CL for benchmark choices of the MSSM parameters [3,4].

A total integrated luminosity of 176.2 ± 0.9 pb^{-1} was recorded by ALEPH in 1998 at a centre-of-mass energy of 188.6 GeV. This higher centre-of-mass energy and integrated luminosity substantially increase the experimental sensitivity for the detection of Higgs bosons.

This paper is organised as follows. The main features of the ALEPH detector are summarised in Sect. 2. Monte Carlo simulations of signal and background processes are presented in Sect. 3. An overview of the search strategy is given in Sect. 4. The event selections for each of the signal final states are described in Sects. 5, with emphasis on features that are new with respect to previously published analyses. Systematic uncertainties are discussed in Sect. 6. The results from individual channels and their combinations are presented in Sect. 7. The MSSM parameter scan beyond the benchmark scenarios, initiated in [4], is updated in Sect. 8. Conclusions follow in Sect. 9.

2 The ALEPH detector

This section summarises the components and performance of the ALEPH detector which are most relevant for the analyses presented here. A more detailed description can be found in [5] and [6].

Three tracking devices are immersed in an homogeneous magnetic field of 1.5 T. The vertex detector (VDET) [7] consists of two cylindrical layers of silicon wafers situ-

ated at average radii of 6.3 and 11.0 cm. Charged particles with a polar angle in the range $|\cos\theta| < 0.88$ (0.95) traverse two (one) VDET layers. The VDET is surrounded by an inner tracking wire chamber (ITC) which provides up to eight r-ϕ hits between radii of 16 and 26 cm. Outside the ITC is the main tracking detector, a large time projection chamber (TPC) which measures up to 21 three-dimensional coordinates per charged particle between radii 31 and 180 cm.

The electromagnetic calorimeter (ECAL) is also situated inside the superconducting coil. It is finely segmented into projective towers of $0.9° \times 0.9°$, allowing the identification of electrons and photons within jets. Luminosity calorimeters of similar construction to ECAL are installed between the endcaps and the beam pipe and are treated as an extension of the calorimeter. A silicon-tungsten sampling calorimeter completes the electromagnetic calorimeter coverage down to 34 mrad.

Outside the coil the hadron calorimeter (HCAL) measures the hadronic energy and acts as a filter for the identification of muons. The outermost detectors are two double layers of muon chambers. Muons are identified as charged particles with a characteristic hit pattern as they traverse the HCAL or with associated hits in the outer chambers.

Charged particle tracks reconstructed with at least four hits in the TPC and originating from within a cylinder of 2 cm radius and 20 cm length centred on the nominal interaction point are called *good tracks*. The tracking achieves a momentum resolution $\sigma(p_T)/p_T$ of $6 \times 10^{-4} \, p_T \oplus 0.005$, with p_T in GeV/c. The resolution on the three-dimensional impact parameter of tracks can be parametrised as $(34+70/p)(1+1.6\cos^4\theta)\,\mu$m, with p in GeV/c.

The measurements of charged particle tracks and of energy depositions in the calorimeters, combined with the identification of photons, electrons, and muons, are used to produce a list of charged and neutral *energy flow particles*. Hadronic jets are clustered from these objects with a resolution approximately described by $\sigma(E) = (0.60\sqrt{E} + 0.6)(1 + \cos^2\theta)$, where E is the jet energy in GeV and θ is its polar angle. The resolution on the jet angles is approximately 20 mrad in both θ and ϕ.

3 Signal and background simulation

High statistics Monte Carlo samples for the signal and backrounds are produced with full simulation of the ALEPH detector, to estimate the signal efficiency and the background level from each relevant Standard Model process. The HZHA generator [8] is used for all the calculations in the Higgs boson sector, with radiative corrections from [9], to produce expected signal cross sections and final state branching ratios for both the hZ and hA processes. For final states with τ leptons, the τ polarisation is transmitted to the TAUOLA library [10] for the subsequent τ decay. For the hZ process, Higgs boson masses are generated in 5 GeV/c^2 steps from 60 GeV/c^2 to 100 GeV/c^2; for the hA process m_h is varied between 75 GeV/c^2 and 95 GeV/c^2 with $m_h = m_A$.

Table 1. Statistics of the simulated samples for Standard Model background processes

Standard Model process	Generator	Cross section (pb)	Simulated luminosity (10^3 pb^{-1})
$e^+e^- \to q\bar{q}(\gamma)$	PYTHIA	99.4	5
$e^+e^- \to ZZ, Z\gamma^*$	PYTHIA	2.76	36
$e^+e^- \to WW$	KORALW	16.5	15
$e^+e^- \to We\nu$	PYTHIA	0.66	23
$e^+e^- \to Zee$	PYTHIA	6.84	36
$e^+e^- \to Z\nu\bar{\nu}$	ZNNB	0.011	910

The PYTHIA Monte Carlo generator [11] is used to simulate the $e^+e^- \to q\bar{q}(\gamma)$ process. For the h$\nu\bar{\nu}$ channel, which is sensitive to initial state radiation modelling, the KORALZ generator [12] is also used to determine the q$\bar{q}$ background level. The difference between the two generators is taken as the theoretical uncertainty.

The Standard Model four-fermion processes are simulated with PYTHIA for $e^+e^- \to ZZ, Z\gamma^*$, and the KORALW generator [13] for $e^+e^- \to WW$. Since the contribution of electrons emitted close to the beam axis in the Weν and Zee processes is not included in KORALW, additional samples for these processes are generated with PYTHIA. The small contribution from the Z$\nu\bar{\nu}$ process is simulated with a private generator ZNNB[14]. The available statistics of the background Monte Carlo samples are given in Table 1, while for the signal Monte Carlo a sample size corresponding to at least 50 times the collected luminosity is used in the analyses at each Higgs boson mass.

4 Search strategy

The main new features of the search with respect to the previous ALEPH analyses [1–4] are the following:

i) full background subtraction is now performed when calculating the limits;
ii) the likelihood ratio test statistic is adopted for limit setting;
iii) the hZ and hA selections are combined taking into account their overlaps.

The previously developed event selections for the various topologies arising from the hZ process, addressing the h$\ell^+\ell^-$ channel (where ℓ denotes either an electron or a muon), the h$\nu\bar{\nu}$ channel, the hq$\bar{q}$ channel, the h$\tau^+\tau^-$ channel and the $\tau^+\tau^-$q$\bar{q}$ channel, which complements the hq$\bar{q}$ channel when h decays to a $\tau^+\tau^-$ pair, are upgraded. Neural Network (NN) and/or cut based event selections are used, as summarised in Table 2. Dedicated selections are applied to the b$\bar{b}$b$\bar{b}$ and b$\bar{b}\tau^+\tau^-$ channels arising from the hA pair production process.

In the h$\ell^+\ell^-$ selection, new cuts are designed to improve the rejection of the W$\ell\nu$ and Zγ^* background events. In final states with τ leptons, the new selection exclusively

Table 2. Final states addressed by each event selection. The crosses indicate which types of event selection are used

Event selection	Decay modes	NN-based	Cut-based
$hq\bar{q}$	$h\to q\bar{q}$, gg	$\times$	$\times$
$h\nu\bar{\nu}$	$h\to q\bar{q}$, gg, $\tau^+\tau^-$	$\times$	$\times$
$h\ell^+\ell^-$	$h\to q\bar{q}$, gg, $\tau^+\tau^-$		$\times$
$h\tau^+\tau^-$	$h\to q\bar{q}$, gg, $\tau^+\tau^-$	$\times$	
$\tau^+\tau^- q\bar{q}$	$h\to\tau^+\tau^-$	$\times$	
$b\bar{b}b\bar{b}$	$h/A\to q\bar{q}$, gg		$\times$
$b\bar{b}\tau^+\tau^-$	$h/A\to q\bar{q}$, gg, $\tau^+\tau^-$	$\times$	

classifies an event as either an $h\tau^+\tau^-$ or $\tau^+\tau^- q\bar{q}$ final state. In the $h\nu\bar{\nu}$ channel, a new preselection is applied, and a new NN-based event selection complementing the previous one is developed. The $hq\bar{q}$ event selection previously based on two neural networks is simplified to a single neural network. The b quark content of jets is evaluated with a NN b tag as in [2], except in the search for the $b\bar{b}b\bar{b}$ final state, where a new NN b tag is designed. In this paper, η_i refers to the b tag NN output of jet i; η_i has a value close to one for b jets, and close to zero for udsc jets.

The likelihood ratio test statistic [15,16] is used to evaluate CLs. This test statistic is optimal in the two-hypothesis situation (signal + background *vs.* background only) addressed here and provides a straightforward procedure for the combination of results in different channels. An analytic method based on fast Fourier transformation is used to calculate the CLs, both for the individual search channels and for the combination of different channels [17].

As in [2], the reconstructed Higgs boson mass is used as a discriminating variable in the calculation of the CLs for all final states. In the NN-based $hq\bar{q}$ channel, the neural network output is used as an additional discriminating variable. Similarly, the b quark content is used in the $h\ell^+\ell^-$ and $b\bar{b}b\bar{b}$ channels.

The various hZ selections are optimised for a Higgs boson of mass $95\,\mathrm{GeV}/c^2$, which is near the expected experimental sensitivity. The hA selections are optimised for $m_h = m_A = 85\,\mathrm{GeV}/c^2$. The cut values on the most relevant selection variables are determined by minimizing the average CL of the "signal + background" hypothesis which is expected when only background is present [18]. For the optimisation procedure, the irreducible backgrounds (ZZ, $Z\nu\bar{\nu}$ and Zee) are fully subtracted, but only 80% of the reducible ones. To derive the final results, full subtraction of all backgrounds is performed according to [19], and systematic uncertainties, both for the signal and the backgrounds, are included in the CL calculation according to [20].

In the $h\nu\bar{\nu}$ channel, two NN-based analyses are combined with the "AND-and-EXCLUSIVES" method described in [2]. This consists in splitting two overlapping analyses into three statistically independent branches, one containing the overlap and the other two the exclusive contributions of the two analyses. The same approach is followed to combine the hZ with the hA selections in the four-jet and the $b\bar{b}\tau^+\tau^-$ topologies. Many background events are common to the hZ and hA selections and it therefore becomes necessary to remove any double counting when background subtraction is performed. For the combination with hA the NN-based hZ analyses are chosen as they give a slightly better overall expected performance. A more general combination including the alternative cut-based hZ analyses is also performed.

5 Event selection

5.1 The leptonic final state

The $h\ell^+\ell^-$ channel represents 6.7% of the Higgsstrahlung cross section. The same final state is produced by the ZZ-fusion process, which has a negative interference with the s-channel process [21]. The signal events are characterised by two energetic leptons with an invariant mass close to m_Z and a recoil mass equal to the Higgs boson mass. Although the branching ratio of this channel is small, the experimental signature is very clear and the Higgs boson mass can be reconstructed with good resolution.

The event selection follows closely that of [2]. The selection procedure attempts to reconstruct the Z boson by finding pairs of leptons. Charged particles are considered as lepton candidates if they are identified as electrons or muons [6] or if they are isolated from other particles by more than $10°$. All accepted combinations of oppositely charged lepton candidates must have at least one identified lepton; e-μ pairs are not considered. The resolution on the Higgs boson mass, calculated as the recoil mass to the lepton pair, is improved by including any recorded final state radiation photons from the Z boson decay products.

The other selection criteria remain unchanged with respect to those published in [2] with the following exceptions. The background from $WW\to q\bar{q}'\ell\nu$ events is rejected by explicitly reconstructing the two W bosons when one of the lepton candidates is identified and the other is an unidentified but isolated charged particle. The identified lepton and the missing four-momentum attributed to the neutrino are assigned to the leptonic W decay, while the remaining energy flow particles are assigned to the hadronic W decay; events with $m_W^{hadr} + m_W^{lept} > 150\,\mathrm{GeV}/c^2$ and $m_W^{hadr} - m_W^{lept} < 20\,\mathrm{GeV}/c^2$ are then rejected. This modification reduces the remaining WW contribution by an additional 30%, leaving the signal unaffected. A new selection cut is introduced to eliminate $Z\gamma^*$ events where the low mass γ^* decays to leptons. Backgrounds from these events occur when one lepton from the γ^* decay is selected along with an unidentified but isolated charged particle from the Z decay. They are eliminated by finding the other identified lepton of the γ^* decay and requiring that the sum of this lepton pair's invariant mass and its recoil mass be greater than $115\,\mathrm{GeV}/c^2$. To remove any potential background from $\ell^+\ell^-\gamma\gamma$ events, both jets of the recoil system are required to contain at least

one charged particle. Finally the requirement on the reconstructed Z boson mass is reoptimised from $m_{\ell^+\ell^-(\gamma)} \geq 82.75\,\mathrm{GeV}/c^2$ to $m_{\ell^+\ell^-(\gamma)} \geq 77.0\,\mathrm{GeV}/c^2$. With these cuts, a 79.5% efficiency is obtained for a Higgs boson of $95\,\mathrm{GeV}/c^2$ mass; 14 events are selected from the data, to be compared with 14.0 expected from Standard Model backgrounds, dominated by ZZ production.

5.2 The missing energy final state

The channel in which the Z decays invisibly to two neutrinos accounts for 20% of the Higgsstrahlung production cross section. The WW-fusion process, which interferes positively with the Higgsstrahlung for high mass of the Higgs boson, enhances the number of expected events. Its relative importance increases with the Higgs boson mass, amounting to 20% of the total $h\nu\bar{\nu}$ final states for a Higgs boson of $95\,\mathrm{GeV}/c^2$ mass [21].

Higgsstrahlung events in which the Z decays to $\nu\bar{\nu}$ are characterised by a missing mass $M̸$ consistent with m_Z and two b-tagged jets from the h decay. Three different analyses have been developed, which share a new preselection. The first one employs a set of cuts on kinematic variables; the other two use neural networks. For b tagging, jets are clustered with the Durham algorithm [22] using $y_{cut} = 0.015$. The neural network b tag is applied to each jet. If there are more than two jets in an event, the two jets with the highest b tag outputs are chosen.

5.2.1 Preselection

For all three analyses, the preselection begins with a selection of hadronic events having five or more reconstructed charged particles and a total energy from all charged particles greater than $10\%\sqrt{s}$. Events are divided into two hemispheres by a plane perpendicular to the thrust axis. Both hemispheres must have a non zero energy.

To reduce the number of events from $\gamma\gamma$ processes, events must have $E_{30°} > 25\%\sqrt{s}$ or $p̸_T > 5\%\sqrt{s}$, where $E_{30°}$ is the energy deposited more than $30°$ away from the beam axis and $p̸_T$ is the transverse component of the missing momentum. The longitudinal component of the missing momentum $p̸_z$ must be small, $|p̸_z| < 50\,\mathrm{GeV}/c$, and the missing mass $M̸$ must be large, $M̸ > 50\,\mathrm{GeV}/c^2$.

After all cuts, the preselection is 85% efficient for a Higgs boson of mass $95\,\mathrm{GeV}/c^2$; $e^+e^- \to$ WW and $e^+e^- \to q\bar{q}$ give the largest contributions to the background.

5.2.2 Cut analysis

Most of the $q\bar{q}$ events remaining after preselection contain one or more unmeasured photons from initial state radiation (ISR). Much of this background is removed by requiring that the missing momentum point away from the beam axis, $\theta_{p̸} > 35°$. Compared to these $q\bar{q}$ events, a large fraction of the Higgs signal events have acoplanar jets. The modified acoplanarity $\tilde{A}$, defined as $\tilde{A} = (\hat{\jmath}_1 \times \hat{\jmath}_2) \cdot \hat{z}$ (where

$\hat{\jmath}_i, \hat{z}$ are unit vectors along the jets and beam directions), must be greater than 0.08.

The WW background after the preselection consists essentially of events in which one W decays into hadrons and the other one into a τ and a neutrino. Such events can be recognised if the τ is well isolated and either decays leptonically or is sufficiently isolated and energetic. Two cuts specifically reject this background: $E_{iso} > 8\,\mathrm{GeV}$ and $\alpha_{iso} < 25°$; E_{iso} is the sum of the energy within $30°$ of the most energetic identified lepton, and the isolation angle α_{iso} is the angle from the most energetic track to its nearest neighbour. To reject Weν and Zee events with an energetic electron deflected at a low angle into the detector, the energy deposited within a cone of $12°$ half angle around the beam axis is required to be small, $E_{12°} < 1.2\%\sqrt{s}$.

The missing mass is required to be greater than $70\,\mathrm{GeV}/c^2$ and the sum of the two b tag NN outputs greater than 1.3. The latter cut also sharply reduces all of the other backgrounds.

After the selection cuts, 7.3 events are expected from Standard Model processes, compared to the eight observed. About 50% of the background comes from ZZ$\to$ b$\bar{\mathrm{b}}\nu\bar{\nu}$, with the rest split between q$\bar{\mathrm{q}}$, WW, and Weν. The efficiency is 35% for a Higgs boson of mass $95\,\mathrm{GeV}/c^2$.

5.2.3 The single-neural-network analysis (A)

This neural network based selection is similar to that used at $\sqrt{s} = 183\,\mathrm{GeV}$[2]. The neural network uses seven variables in common with the preselection and the cut selection: $E_{30°}$, $|p̸_z|$, $M̸$, $\theta_{p̸}$, $\tilde{A}$, $E_{12°}$, $\eta_1 + \eta_2$, and five additional ones. The additional variables include the fraction f_{wedge} of the centre-of-mass energy within a $\pm 30°$ azimuthal wedge centred on the missing momentum direction, the acollinearity A of the jets, the energy E_τ of the most isolated minijet, *i.e.* a jet with invariant mass less than $2\,\mathrm{GeV}/c^2$ as expected for taus, and a combination of the b tagging variables, $\log_{10}((1-\eta_1)(1-\eta_2))$. The reconstructed Higgs boson mass M_{rec} is also included as an input.

This NN, with a 12-20-3 structure, is trained to discriminate the signal from the WW and q$\bar{\mathrm{q}}$ backgrounds. Figure 1a shows the neural network output distribution. The result of the optimisation procedure leads to a NN cut value of 0.966. A signal efficiency of 33% is obtained for $m_h = 95\,\mathrm{GeV}/c^2$, with a predicted background of 3.9 events. Five candidates are selected from the data.

5.2.4 The three-neural-network analysis (B)

This new analysis treats independently the two main backgrounds, q$\bar{\mathrm{q}}$ and WW, allowing valuable cross checks to be performed on the systematic uncertainties implied by the background subtraction. Each of the backgrounds, q$\bar{\mathrm{q}}$ and WW, is addressed by a set of cuts and by a dedicated NN involving only kinematic variables. To discriminate the signal from all Standard Model backgrounds, a third neural network is used, with four input variables: the two
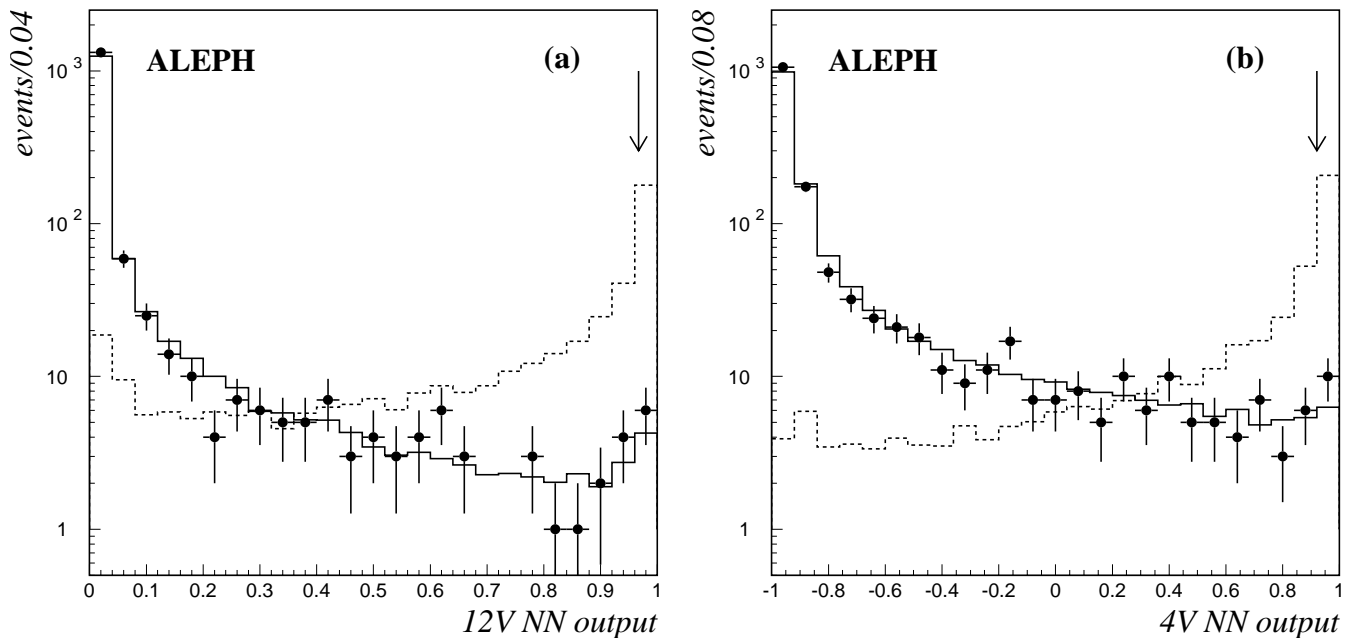
Fig. 1a,b. Distributions of **a** the 12-variable NN output and **b** the 4-variable NN output used to select $h\nu\bar{\nu}$ events, for the data (dots with error bars) and simulated backgrounds (histograms). The expected Higgs boson signal for $m_h = 95\,\mathrm{GeV}/c^2$ is also shown as dashed histograms with arbitrary normalisation. The arrows indicate the cuts above which events are selected

aforementioned dedicated NN outputs and the b tag NN outputs for the two best b-tagged jets.

The few remaining non-radiative $q\bar{q}$ events after the general preselection are eliminated by the cut $\not{M} > M_{\mathrm{vis}} - 50\,\mathrm{GeV}/c^2$, where M_{vis} is the visible mass. This cut results in a loss of 0.4% in signal efficiency. A seven-variable NN, with a 7-5-3-2 structure, is then trained to discriminate the signal and the $q\bar{q}$ background. The input variables are similar, although not identical, to those used in the cut-based and single-NN approaches. The variables chosen are $\not{M}$; $\theta_{\not{p}}$; $\not{p}_T$; $E_{30°}$; f_{wedge}; $\Delta\phi$, the azimuthal angle between the two hemisphere momenta; s'/s, reconstructed from the jet directions as defined in [23].

Half of the WW background remaining after the preselection is removed by the requirements $E_{\mathrm{iso}} > 5\,\mathrm{GeV}$ and $E_\tau < 10\,\mathrm{GeV}$. These cuts reduce the signal efficiency by 1.4%. A three-variable NN, with a 3-5-3-2 structure, is then trained to discriminate the signal and the WW background. The input variables are the missing mass $\not{M}$, the jet acollinearity A, and the total missing momentum $\not{p}$.

To further discriminate the signal from the $q\bar{q}$ and WW backgrounds, and also to reduce the other Standard Model background sources, the b hadron content of the two best b-tagged jets is used. Therefore, the two b tag NN outputs ordered by increasing values, and the outputs of the anti-$q\bar{q}$ and anti-WW NNs described above, are input to a four variables NN, with a 4-5-3-2 structure. Furthermore, the background training sample is composed of all the relevant Standard Model processes ($q\bar{q}$, WW, Weν, Zee, and ZZ), except for the irreducible ZZ$\rightarrow$b$\bar{\mathrm{b}}\nu\bar{\nu}$ background, in proportion to their cross sections. Figure 1b shows the neural network output distribution. Finally, af-

ter investigation of the level of beam related background in the data, the cut $E_{12°} < 3.5\% \sqrt{s}$ is applied.

The optimisation procedure results in a cut value on the NN output of 0.921. With this cut value, a signal efficiency of 40% is obtained for $m_h = 95\,\mathrm{GeV}/c^2$ and 5.5 events are expected from background processes. Nine candidate events are selected from the data, of which five are in common with the single NN selection, and seven with the cut-based analysis.

5.3 The four-jet final state

The hq$\bar{\mathrm{q}}$ final state accounts for 64.6% of the Higgsstrahlung cross section. The four-jet topology is selected by cut- and NN-based analyses which share common event preselection criteria. Events are required to have at least eight good tracks satisfying $|\cos\theta| \leq 0.95$. Radiative returns to the Z resonance are rejected when the initial state photon is observed in the apparatus as well as when it escapes down the beam pipe as described in [1]. The events are then forced to four jets with the Durham jet-clustering algorithm [22]. The y_{cut} value y_{34} at which the transition from four to three jets occurs must be larger than 0.004. Each jet is required to contain at least one good track. The jet four-momenta are rescaled to comply with energy-momentum conservation, keeping the jet angles and velocities to their measured values.

5.3.1 Event selection with cuts

The event selection is an update of that described in [2]. The sum Θ of the four smallest interjet angles in the event

is required to be larger than $350°$. The sensitivity of the selection is designed to be close to the hZ production threshold and therefore the WW and $q\bar{q}gg$ backgrounds can be reduced by requiring that events have two pairs of nearly back-to-back jets. In practice, this topology is selected by requiring $\gamma = \min(\cos\theta_{ij} + \cos\theta_{kl}) < -1.30$, with minimisation over all permutations of jet indices $ijkl$.

In events with four jets there are six different ways of assigning one di-jet to the Higgs candidate and the other di-jet to the Z candidate. The following selection criteria are applied to all such pairings. The selection is subdivided into two parts, (a) and (b) defined below, designed to select hZ→$b\bar{b}q\bar{q}$ and $b\bar{b}b\bar{b}$ events, respectively. An event is selected if at least one jet pairing passes all the above cuts as well as either (a) or (b).

In order to select hZ→$b\bar{b}q\bar{q}$ events, four well-separated jets are required, and additional cuts are applied to the invariant masses of the Higgs and Z boson di-jet candidates, as well as to the b quark content of the Higgs candidate jets:

(a) • $y_{34} > 0.008$;
   • $m_{12} > 64\,\mathrm{GeV}/c^2$ (Z candidate jets);
   • $m_{34} > 55\,\mathrm{GeV}/c^2$ (Higgs candidate jets);
   • $\min(\eta_3, \eta_4) > 0.40$ (Higgs candidate jets);
   • $(1-\eta_3)(1-\eta_4) < 7.6 \times 10^{-3}$ (Higgs candidate jets).

The hZ→$b\bar{b}b\bar{b}$ selection is based on a linear combination of the b tag information for the four jets and the information about the separation between the jets:

(b) $9.5y_{34} + \sum_{i=1}^{4}\eta_i > 3$.

The above selection criteria are applied to all six jet pairings in the event. In the overwhelming majority of cases, for events passing the cuts (a) only one jet pairing is selected. The linear discriminating variable in (b) is independent of the choice of jet pairing. For events passing selection (b) all six pairings are kept.

If more than one jet pairing is selected for a given event, one pairing must be chosen for use in the discriminating variable — the reconstructed Higgs boson mass $m_h = m_{12} + m_{34} - m_Z$ — which is required for the calculation of the CLs. One possible criterion [2] is to choose the pairing for which m_{12} is closest to the nominal Z boson mass. For type (b) events, this method has a non-negligible probability of selecting an incorrect pairing and thus reduces the discriminating power of m_h. Given that most of the signal events selected by cuts (b) are hZ→$b\bar{b}b\bar{b}$, one cannot improve the choice of pairing by using the b tagging information of the jets. The choice of pairing is improved with respect to [2] by using the decay angles of the Z and Higgs boson di-jet candidates (α_{12} and α_{34}, respectively) instead of m_{12}. A probability density function $P(\alpha_{12}, \alpha_{34})$, that reflects the differences between the correct signal pairing and the incorrect pairings (for signal and backgrounds), is built. The pairing with the largest probability is selected. This has the effect of increasing the reach in m_h of the four-jet selection by $\sim 0.5\,\mathrm{GeV}/c^2$ with respect to the previously used pairing choice.

With the set of cuts derived through the optimisation procedure, the signal efficiency is 39.4% for a Higgs boson

of $95\,\mathrm{GeV}/c^2$ mass. Twenty-four candidates are selected from the data, to be compared with 19.0 events expected from Standard Model processes.

5.3.2 Event selection with a neural network

A neural network is trained to identify the hZ→$b\bar{b}q\bar{q}$ signal while rejecting the $q\bar{q}$ and WW background processes. This approach represents a simplification with respect to that followed in [2]; the two NNs, one anti-$q\bar{q}$ and one anti-WW, have been merged into a single NN with a 17-30-1 structure which leads to comparable performances with respect to that in [2].

The general NN features remain similar to those used in [2]. For the training phase, the NN is presented with up to six different di-jet pairings per background event, and only one, the correct pairing, per signal event. The training uses only events surviving the preselection described in Sect. 5.3, complemented with the requirement $\sum_{i=1}^{4}\eta_i > 1$. In addition, di-jet pairings with $m_{34} < 45\,\mathrm{GeV}/c^2$ are discarded. A mixture of Monte Carlo signal events with $m_h = 80, 85, 90$ and $95\,\mathrm{GeV}/c^2$ is used to achieve good performance over the range of masses relevant for the MSSM, while for the background the WW and $q\bar{q}$ processes are used. The inputs to the neural network include several of the selection variables used in the cut-based analysis: y_{34}, γ, m_{12}, Θ, $\min(\eta_3, \eta_4)$, $(1-\eta_3)(1-\eta_4)$, and $\sum_{i=1}^{4}\eta_i$.

Additional kinematic variables are included in the NN. An event broadening observable B, described in [2], offers discriminating power between signal and background events. Other kinematic variables, such as the largest jet energy $E_{\max}$ and the two smallest jet energies $E_{\min}$ and $E_{\min2}$, are also included. Several observables offer discriminating power between light quark and gluon jets for the two Z candidate jets. The boosted sphericity calculated in the rest frame of the jet and the multiplicity of tracks with rapidity larger than 1.6 with respect to the jet axis are included as well as the two minimum jet masses.

Distributions of the NN output are shown in Fig. 2 for signal, background, and data.

An event is selected if at least one of its jet pairings has a NN output greater than 0.951. If more than one di-jet combination in an event passes this criterion, the combination with the highest NN output is chosen. The resulting signal detection efficiency for a Higgs boson signal with mass $95\,\mathrm{GeV}/c^2$ is 46.0%. The expected number of background events is 21.4 (6.2 from $q\bar{q}$, 4.2 from WW, and 11.0 from ZZ); 28 candidate events are selected in the data. Among them, 19 are in common with those selected by the cut-based analysis described in Sect. 5.3.1, in agreement with expectations from the simulation.

5.4 The four-b final state

The $b\bar{b}b\bar{b}$ final state arising from the hA production is characterised by a four-jet topology and a high b quark content. The preselection is unchanged with respect to
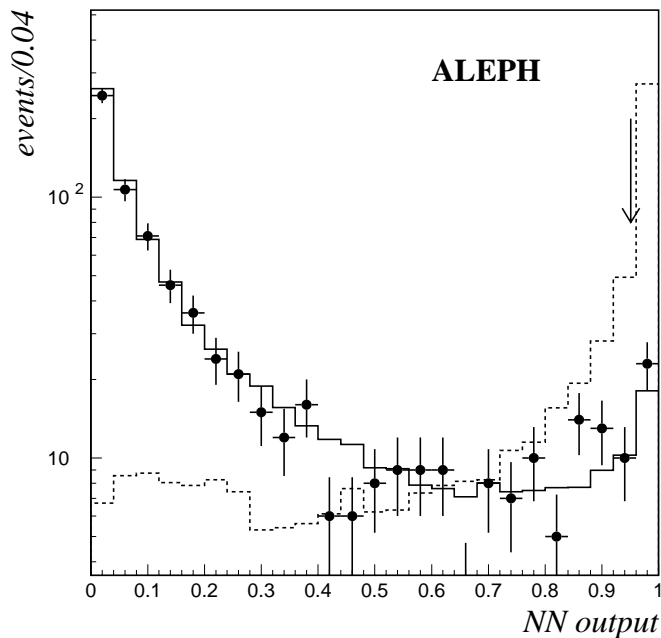
Fig. 2. Distributions of the NN output used to select four-jet hZ candidates for data (dots with error bars), simulated background (histogram), and simulated Higgs signal for $m_h = 95\,\mathrm{GeV}/c^2$ (dashed histogram). The signal histogram has an arbitrary normalisation. The arrow shows the cut value above which events are selected

[4]. At this level the main contributions to the background come from the ZZ, WW, and q$\bar{q}$ processes. The b tag information is essential for the rejection of these backgrounds and a new four-variable b tag NN is used in this channel. Three of the variables are the same as in the NN used in [4]: the confidence level $\mathcal{P}_{\mathrm{uds}}$ of a jet being a light quark jet based upon impact parameters of tracks in the jet, the χ^2 difference $\Delta\chi^2_{\mathrm{svx}}$ between a fit assuming that all tracks in the jet originate from the primary vertex and a fit assuming that a secondary vertex exists, and the transverse momentum p_{T} of identified leptons with respect to the jet axis. The fourth variable is the scaled inclusive X_{E}, defined as the fraction of the jet energy carried by the most energetic particles which have a total invariant mass smaller than $2.1\,\mathrm{GeV}/c^2$. This b tag NN achieves, at 55% signal efficiency, a 20% improvement on the background rejection with respect to the previous three-variable neural network.

The final event selection is based upon the combination $\mathcal{F}$ of the minimum di-jet angle, $\theta_{ij}^{\mathrm{min}}$, and the b quark content, defined as

$$\mathcal{F} = 300 \times \left(4 - \sum_{j=1}^{4} \eta_j\right) - \theta_{ij}^{\mathrm{min}}.$$

The $\mathcal{F}$ distribution is shown in Fig. 3. The discrepancy between data and simulation for high values of $\mathcal{F}$ is also observed in other ALEPH analyses [24]. The data distribution is broader than the simulated one; this is understood to be due to slight inadequacies in the b tag simulation,
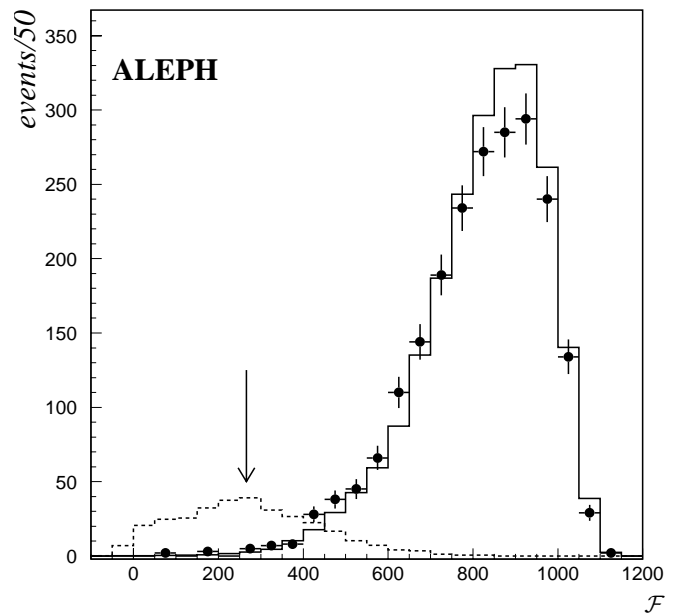

Fig. 3. Distribution of the $\mathcal{F}$ variable for data (dots with error bars), simulated background (histogram), and simulated Higgs signal for $m_h = m_A = 85\,\mathrm{GeV}/c^2$ (dashed histogram) at the preselection level. The signal histogram has an arbitrary normalisation. The arrow indicates the cut value below which events are selected

as discussed in Sect. 6.1. The optimisation procedure leads to the cut $\mathcal{F} < 266$, corresponding to a signal efficiency of 49.1% for $m_h = m_A = 85\,\mathrm{GeV}/c^2$ and a background expectation of 4.8 events (2.7 q$\bar{q}$, 2.0 ZZ, 0.1 WW). Seven candidates are selected in the data.

5.5 Final states with τ leptons

The h$\tau^+\tau^-$ final state corresponds to 3.4% of the total Higgsstrahlung process, and h $\rightarrow \tau^+\tau^-$, Z$\rightarrow$q$\bar{q}$ corresponds to an additional 5.5%. In the case of e$^+$e$^-\rightarrow$hA, about 15.5% of the final states are $\tau^+\tau^-$b$\bar{b}$. The event topology consists of two hadronic jets and two oppositely charged, low multiplicity jets with missing energy due to the neutrinos from the τ decays. The h $\rightarrow \tau^+\tau^-$, Z $\rightarrow \ell^+\ell^-$ final state is covered in the h$\ell^+\ell^-$ analysis.

5.5.1 Preselection and τ lepton identification

Hadronic events are selected by requiring at least eight good charged tracks and a total energy from all charged particles greater than $20\%\sqrt{s}$. WW and ZZ backgrounds are suppressed by rejecting those events having an identified lepton with energy greater than $25\%\sqrt{s}$. Radiative returns to the Z peak, characterized by high missing energy $\not{E}$ and high missing longitudinal momentum $\not{p}_z$, are rejected by requiring $|\not{p}_z| + \not{E} < 1.8\gamma_{\mathrm{peak}}$ where $\gamma_{\mathrm{peak}} \equiv \sqrt{s}/2 - m_Z^2/(2\sqrt{s})$ is the most likely energy of an initial state radiation photon. To further suppress radiative returns, $|\not{p}_z| < 60\%\gamma_{\mathrm{peak}}$ is also required.
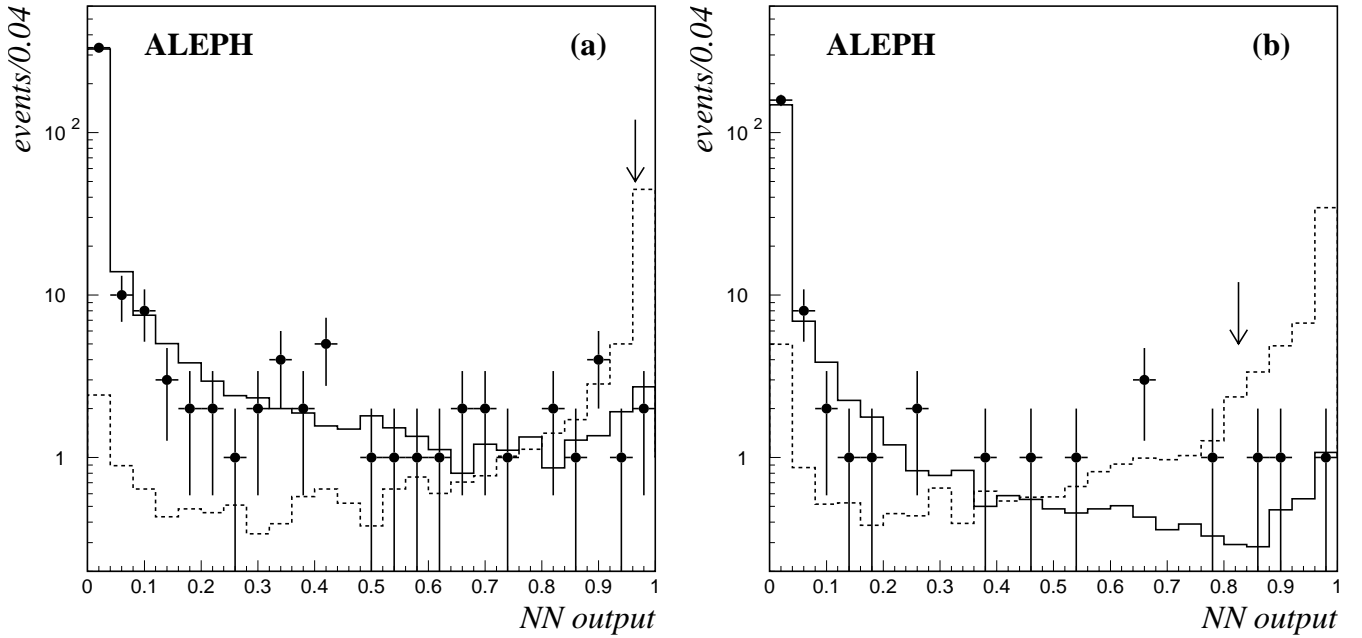
Fig. 4a,b. Distributions of the NN outputs **a** used in the selection of the hZ final states with τ leptons and **b** used in the selection of the hA$\rightarrow$b$\bar{\text{b}}\tau^+\tau^-$ final state for the data (dots with error bars) and the simulated background (histogram). Also shown by the dashed histograms with arbitrary normalisation are the simulated hZ signal for $m_{\text{h}} = 95\,\text{GeV}/c^2$ in **a**, and the hA signal for $m_{\text{h}} = m_{\text{A}} = 85\,\text{GeV}/c^2$ in **b**. The arrows indicate the cut values above which events are selected

Events passing the preselection cuts are clustered into minijets with invariant mass smaller than $2.7\,\text{GeV}/c^2$, consistent with the τ hypothesis. The τ candidates are selected from these minijets using a series of quality cuts based on multiplicity, isolation and momentum as described in [4]. Fully leptonic τ decays are included.

Only events with at least two τ candidates are considered further. The rest of the event is clustered into two jets using the Durham algorithm. All four jets in the event are rescaled using a kinematic consistency fit in which the jet directions are fixed and the minijet masses are set to m_τ. The fit estimator χ^2 is calculated from energy-momentum conservation, hadronic jet resolutions, and the compatibility of the di-jet invariant masses with the assumed final state. In the case of $e^+e^-\rightarrow$hZ, two different fit terms are constructed for the two hZ $\rightarrow \tau^+\tau^-$q$\bar{\text{q}}$ decay modes. In the $h\tau^+\tau^-$ fit, the invariant mass of the τ minijets is compared with m_{Z}, whereas in the $\tau^+\tau^-$Z fit, the invariant mass of the hadronic jets is compared to m_{Z}. For $e^+e^-\rightarrow$hA, assuming that h and A have almost equal masses, the fit term compares the invariant masses of the hadronic and the $\tau^+\tau^-$ systems. In no case are the hadronic jets allowed to rescale to less than 75% of their measured momenta. Events failing the kinematic fit are rejected. A typical event may have several possible combinations of potential τ minijet candidates; only the combination with the smallest kinematic χ^2 is considered further.

5.5.2 hZ final states

To discriminate between $h\tau^+\tau^-$ events, $\tau^+\tau^-$q$\bar{\text{q}}$ events and background events, two NNs are employed. Both NNs take as input the following variables: the kinematic fit estimator χ^2, the event transverse momentum p_{T}, the sum of the two τ minijet isolation angles, defined as the half-angle of the largest cone around the minijet direction containing no more than 5% of the total event energy outside the cone, and the sum of the fitted transverse momenta P_T^{jet} of the τ minijets with respect to the nearest hadronic jet.

To take advantage of the large probability for h to decay to b$\bar{\text{b}}$, the $h\tau^+\tau^-$ NN uses the sum of the NN b tagging outputs of the two hadronic jets as a fifth input variable. The neural networks are trained to discriminate the signal from the q$\bar{\text{q}}$, WW and ZZ background processes. The signal events include Higgs bosons with masses of 85, 90 and $95\,\text{GeV}/c^2$.

Some events, especially those with reconstructed Higgs boson masses near m_{Z}, may be selected by more than one NN selection. A new selection extension based on the NN outputs exclusively classifies an event as either $h\tau^+\tau^-$ or $\tau^+\tau^-$q$\bar{\text{q}}$. Both NN outputs are calculated for each event, and the higher output determines the event classification. If the sum of the two NN outputs is greater than 1.8, the difference between the outputs is small, and the kinematic fit estimator χ^2 is used to distinguish the two signal classes. A slight offset in the χ^2 cut favours classification as $h\tau^+\tau^-$ because the event must have a high b content in order to have two high NN output values. If $\chi^2_{h\tau\tau} - 1 > \chi^2_{\tau\tau q\bar{q}}$, the event is classified as $h\tau^+\tau^-$; otherwise it is classified as $\tau^+\tau^-$q$\bar{\text{q}}$.

In principle, the cut values on the two NN outputs could be varied independently; however it has been found that a single cut, applied to both NN outputs, gives nearly the same selection performance as two independent cuts.
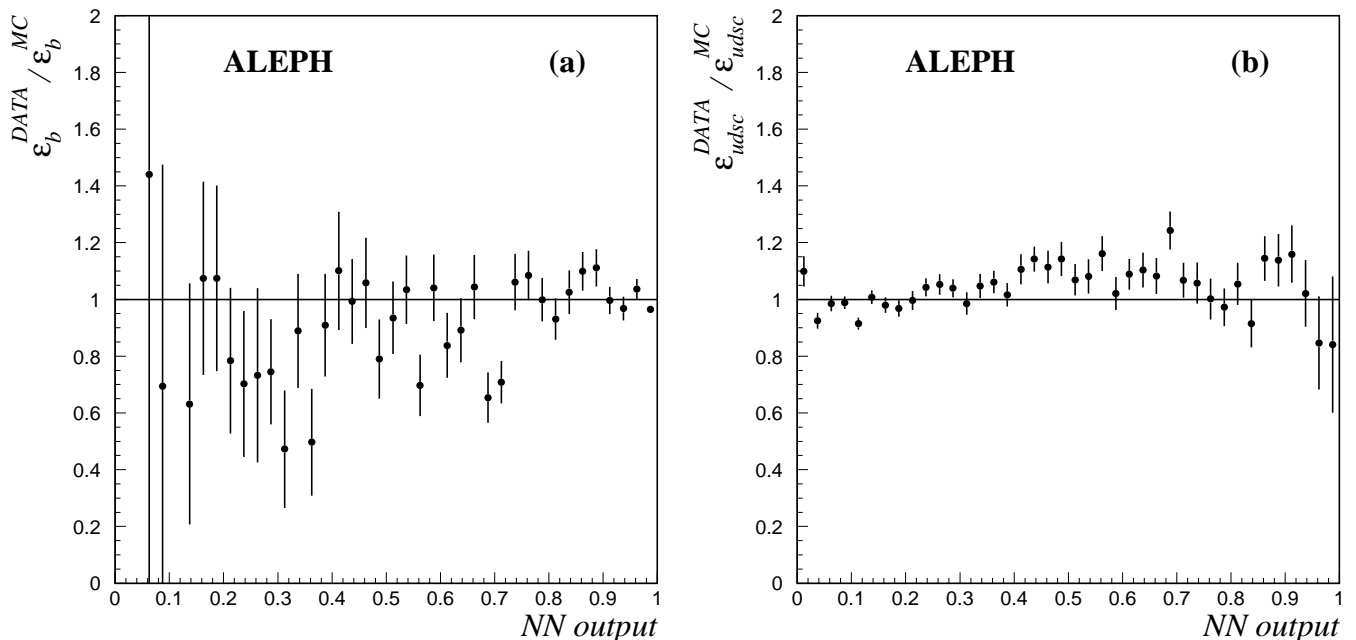
Fig. 5a,b. Comparisons of **a** b tag efficiency and **b** mistag rate between Z peak data and Monte Carlo as a function of the b tagging NN output

To calculate CLs, the expected number of signal events and the shapes of the reconstructed Higgs boson mass distributions are entered separately for the $h\tau^+\tau^-$ and $\tau^+\tau^-q\bar{q}$ classifications. The distribution of the selected NN output is shown in Fig. 4a.

The optimisation procedure leads to a NN cut value of 0.965. For this cut value and assuming $m_h = 95\,\text{GeV}/c^2$, 0.3 $h\tau^+\tau^-$ events and 0.4 $\tau^+\tau^-q\bar{q}$ events are expected, corresponding to signal efficiencies of 29.5% and 17.4%, respectively. The total Standard Model background expectation is 2.5 events. Two candidates are selected from the data.

5.5.3 hA final state

A five-variable NN is also used with the same variables as for the $h\tau^+\tau^-$ selection. The only difference is that the hA signal Monte Carlo is used for the NN training, with $m_A = m_h = 85\,\text{GeV}/c^2$. The distribution of the NN output is shown in Fig. 4b.

The optimisation procedure results in a cut on the neural network output of 0.826. A signal efficiency of 42.0% for $m_A = m_h = 85\,\text{GeV}/c^2$ is obtained, and 2.5 events are expected from Standard Model processes. Three candidates are selected from the data, of which one is shared with the hZ event selection.

6 Systematic uncertainties

Systematic errors stem from uncertainties and inaccuracies in the Monte Carlo simulation. Those concerning b

tagging performance and jet energy and direction reconstruction affect all channels and are discussed first. Systematic uncertainties pertaining specifically to each channel are reported afterwards. Whenever possible, systematic errors are extracted from about $2\,\text{pb}^{-1}$ of data taken at the Z peak during the same year.

6.1 b-tag-related systematic errors

A disagreement between data and Monte Carlo simulation in the tagging efficiency for b jets would affect the acceptance for signal and most background processes. Using the single and double tag method as for the ALEPH R_b analysis [25], the efficiencies for b jets (ϵ_b) and udsc jets (ϵ_{udsc}) are measured directly from two-jet hadronic events collected in 1998 at the Z peak. These efficiencies are compared with those obtained from Monte Carlo simulation; their ratios are displayed in Fig. 5 as a function of the NN b tag output. The discrepancy between data and Monte Carlo indicates that udsc jets are 10% more likely to be identified as b jets in the data than in the Monte Carlo simulation. This is confirmed by a study of the effect of b tagging on semileptonic WW events and radiative Z returns in data taken at $\sqrt{s} = 189\,\text{GeV}$.

For the signal and the ZZ and $q\bar{q}$ backgrounds, the Higgs candidate jets after selection come primarily from b quarks. The main source of b tag related systematic errors is the imperfect simulation of the b tag efficiency. These are evaluated by reweighting the Higgs candidate jets in the Monte Carlo based on their NN b tag outputs according to Fig. 5a. The resulting changes to the selection efficiencies for signal and background processes with respect to the unweighted efficiencies are taken as system-

atic uncertainties. For the WW and Weν backgrounds, the Higgs candidate jets are udsc jets mistagged as b jets. To estimate the systematics from imperfect simulation of this mistag rate, the Higgs candidate jets are similarly reweighted according to Fig. 5b.

As a cross check, tracking parameters are smeared to bring the Monte Carlo simulation of the b tagging closer to the data. The changes in signal and background efficiencies are similar to those obtained by the reweighting method. In a conservative way, discrepancies in b tagging between data and Monte Carlo are included as systematic errors, and not corrected. The effect from the uncertainty of b hadron lifetime, b decay multiplicities or b jet fragmentation has been checked to be much smaller than detector effects.

6.2 Systematic errors related to jet energy and angle

The systematic errors related to the simulation of jet energies and directions are also evaluated from the sample of hadronic events collected at the Z peak in 1998. These studies are done both on jets with and without flavour selection, in order to separately evaluate the systematic uncertainties related to those jets originating from b quarks. To avoid possible biases from the jet shape variables, which enter the NN b tag, the flavour selection criterion is based on the probability of the jet to be a light quark jet based on signed impact parameters ($\mathcal{P}_{uds} < 10^{-3}$).

The energy resolution and calibration are first investigated. Inhomogeneities of the detector response are taken into account by studying separately the barrel ($|\cos\theta| \leq 0.8$) and endcap ($|\cos\theta| > 0.8$) regions. To bring data and Monte Carlo into better agreement, the Monte Carlo jet energies E_{sim} are modified according to the relation $E_{smear} = (1+c)(1+G(\sigma))E_{sim}$, where $G(\sigma)$ is a Gaussian random variable of width σ. For generic jets (b jets), the calibration coefficient c is 0.2% (0.8%) in the barrel and 2.1% (2.2%) in the endcaps. A smearing of $\sigma = 2\% (3\%)$ is applied in the endcaps. No such smearing is necessary in the barrel. The jet masses and momenta are corrected in the same way, keeping the velocities unchanged.

A comparison of the data and Monte Carlo shows that the resolution on the azimuthal and polar angles is systematically too good in the simulation. To improve the agreement, $G(\sigma_\theta)$ and $G(\sigma_\phi)/\sin\theta_{sim}$ smearing terms are added to the polar and azimuthal angles of each Monte Carlo jet respectively. The difference between data and Monte Carlo is minimised for $\sigma_\phi = 0.15° (0.3°)$ and $\sigma_\theta = 0.2° (0.3°)$.

In addition to correcting the simulation, a systematic uncertainty on the selection efficiencies amounting to half of the corrections is adopted.

6.3 The leptonic final state

Potential sources of systematic uncertainties including lepton identification, lepton isolation, and energy and momentum reconstruction are investigated as in [2]. The total relative systematic uncertainties are 0.6%, 2.6%, 7.5%

on the signal efficiency and on the ZZ and Zee backgrounds, respectively. The systematic uncertainties on all the other background processes, WW, Weν and q$\bar{q}$, are dominated by the statistics of the Monte Carlo samples and are smaller than 30% for each of these backgrounds.

6.4 The missing energy final state

Systematic effects related to b tagging and to jet energy and angle measurements are estimated as described in Sects. 6.1 and 6.2. The $E_{12°}$ variable is sensitive to beam related background, which is not simulated. The energy distribution of this background is measured with events triggered at random beam crossings. Additional energy depositions at angles below 12° are randomly added to all Monte Carlo events according to this energy distribution. Half of the correction, amounting to 2% for the signal and for the ZZ background, 5% for the q$\bar{q}$ background and 10% for the WW background, is taken as systematic uncertainty. The three-neural-network analysis, which treats independently the main background contributions, is used as described in [26] in order to cross check the evaluation of the systematic uncertainties pertaining to reducible backgrounds such as q$\bar{q}$ with two ISR photons, WW and Weν. The relative uncertainty in the total selection efficiency is typically 5% for the signal and 10% for ZZ, and it is between 30% and 100% for the other background processes.

6.5 The four-jet and four-b final states

In addition to the common systematic effects described in Sects. 6.1 and 6.2, additional sources of systematic uncertainties affecting the signal and background selection efficiencies are studied. Possible inaccuracies in the simulation of the selection variables ($y_{34}, \gamma, \Theta, m_{12}, m_{34}$), obtained from a bin-by-bin comparison of distributions in the data and simulation, are taken into account using a reweighting technique as for the evaluation of b tag systematic uncertainties. The g$\rightarrow$b$\bar{b}$ splitting rate is corrected to its measured value [27] with a 50% uncertainty. A 5% uncertainty on the strong interaction coupling constant α_s is included for the q$\bar{q}$ background.

For the b$\bar{b}$b$\bar{b}$ final state, the systematic uncertainty related to the signal amounts to 4.2% and is dominated by the b tag. The q$\bar{q}$ background uncertainty is dominated by the uncertainty on the rate of gluon splitting to heavy quarks, which amounts to 30% of the accepted q$\bar{q}$ background. The ZZ background is affected by the same systematic error as the signal, resulting in a 10% uncertainty. The small WW contribution (0.1 ± 0.1 events) to the background has a large statistical error, and a systematic uncertainty of 100% is assigned to this process.

For the b$\bar{b}$q$\bar{q}$ final state, the relative uncertainties on the selection efficiencies are estimated in a similar way to be 3% for the signal, 10% for ZZ, 15% for WW, and 15% for q$\bar{q}$.
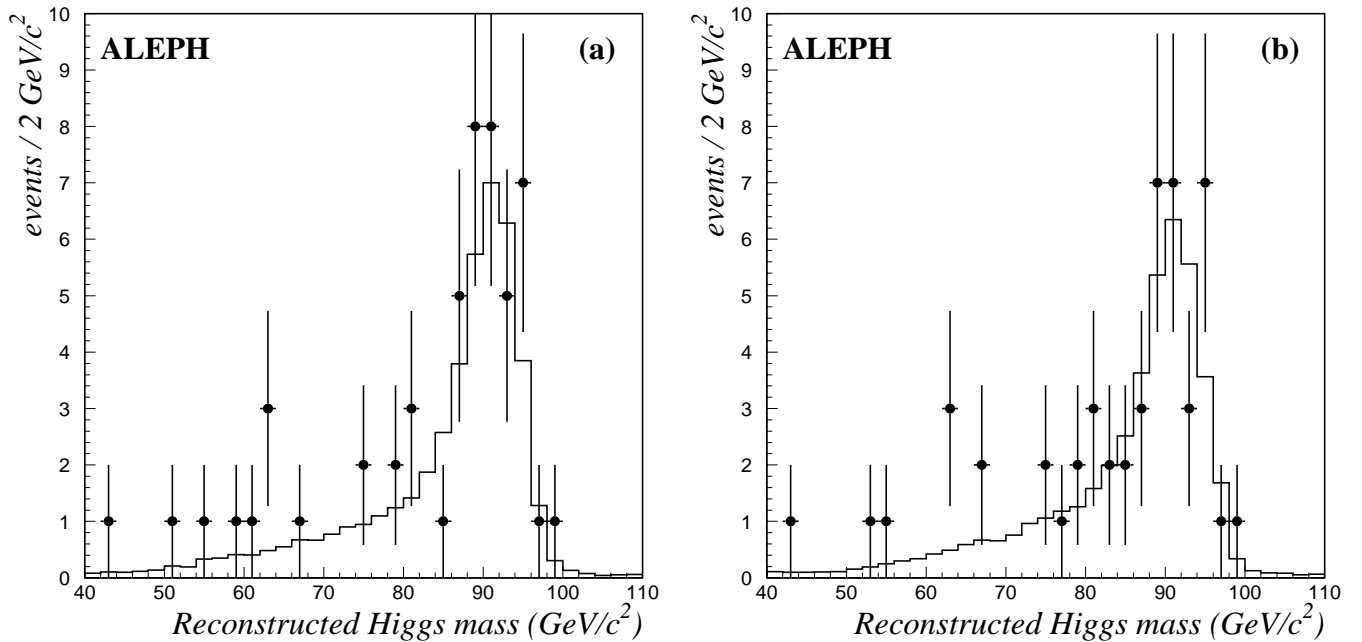
Fig. 6a,b. Distributions of the reconstructed Higgs boson mass for the data events (dots with error bars) selected in the hZ searches by **a** the NN- and **b** the cut-based sets of selections. The histograms show the Standard Model background expectation

6.6 Final states with τ leptons

A systematic effect in the $\tau^+\tau^-$ selections is the uncertainty on the jet angles and therefore on the calculated invariant masses. This effect is studied by applying the procedure described in Sect. 6.2. The effect of the b tagging uncertainty is estimated as explained in Sect. 6.1. For the backgrounds, the dominant uncertainty comes from the limited Monte Carlo statistics used to calculate efficiencies.

Altogether, the systematic uncertainties are smaller than 5% for the signal, 10% for the ZZ background, 20% for WW and 50% for q$\bar{\text{q}}$.

7 Combination and results

As mentioned in Sect. 4, two sets of selections, NN- and cut-based, are used. To cover all hZ final states, the h$\ell^+\ell^-$ analysis is included in the NN-based selection while the h$\tau^+\tau^-$/$\tau^+\tau^-$q$\bar{\text{q}}$ analyses are also used in the cut-based selection. Altogether, 48 (53) events are selected in the data by the hZ selections performed with the cut-based (NN-based) selections, in agreement with the expectation of 42.8 (44.1) events from Standard Model processes. Table 3 summarises, for each set of selections, the expected number of signal events, the expected number of background events, and the number of events selected in the data. Figures 6a and b show the reconstructed Higgs boson mass distributions for the selected candidates and the background expectations from the simulation. These figures combine channels with rather different mass resolutions and are given for illustration purposes only; in par-

ticular the b quark content of individual events is not reflected in the mass plot.

The hA selection yields ten candidate events, of which five are in common with the hZ selection, to be compared with 7.5 background events expected from Standard Model processes.

No significant excess of candidate events is observed. The analyses are therefore used to set 95% CL mass lower limits. In the absence of signal, the mass lower limits expected for the Standard Model Higgs boson are $95.4\,\text{GeV}/c^2$ for the cut-based combination and $95.8\,\text{GeV}/c^2$ for the NN-based combination. Since the NN-based combination yields a slightly better expected limit for hZ searches, it is used in the hZ/hA combination to produce limits in the MSSM plane $[m_\text{h},\sin^2(\beta-\alpha)]$. Furthermore the Standard Model limit, which is effectively obtained for $\sin^2(\beta-\alpha)=1$, benefits from the combination of the hZ and hA selections.

The hZ and hA selections are combined with the "AND-and-EXCLUSIVES" method, taking into account the overlaps in the four-jet and tau analyses, and compared with signals expected from either or both hZ and hA production. The information about the statistically independent branches is summarised in Table 4. An additional complication arises from the use of different discriminating variables in the CL computation. The variable chosen for the overlap branch is the one giving the best expected exclusion CL, and can vary in different regions of the $[m_\text{h},\sin^2(\beta-\alpha)]$ plane. For example, in the four-jet selections, at $\sin^2(\beta-\alpha)=1$ the hZ$\rightarrow$hq$\bar{\text{q}}$ variables are used everywhere, while at $\sin^2(\beta-\alpha)=0$ the hA$\rightarrow$b$\bar{\text{b}}$b$\bar{\text{b}}$ variables are used for $m_\text{h}\le 86\,\text{GeV}/c^2$ and the hZ$\rightarrow$hq$\bar{\text{q}}$ variables for $m_\text{h}>86\,\text{GeV}/c^2$.

Table 3. Expected numbers of signal events (n_s) for a Higgs boson of 95 GeV/c^2 mass, and background events (n_b) from Standard Model processes for the relevant channels of the hZ search. The numbers of events selected in the data (n_{obs}) are also given. For the NN-based selections in the h$\nu\bar{\nu}$ channel, the information is given for the three statistically independent branches of the "AND-and-EXCLUSIVES" method

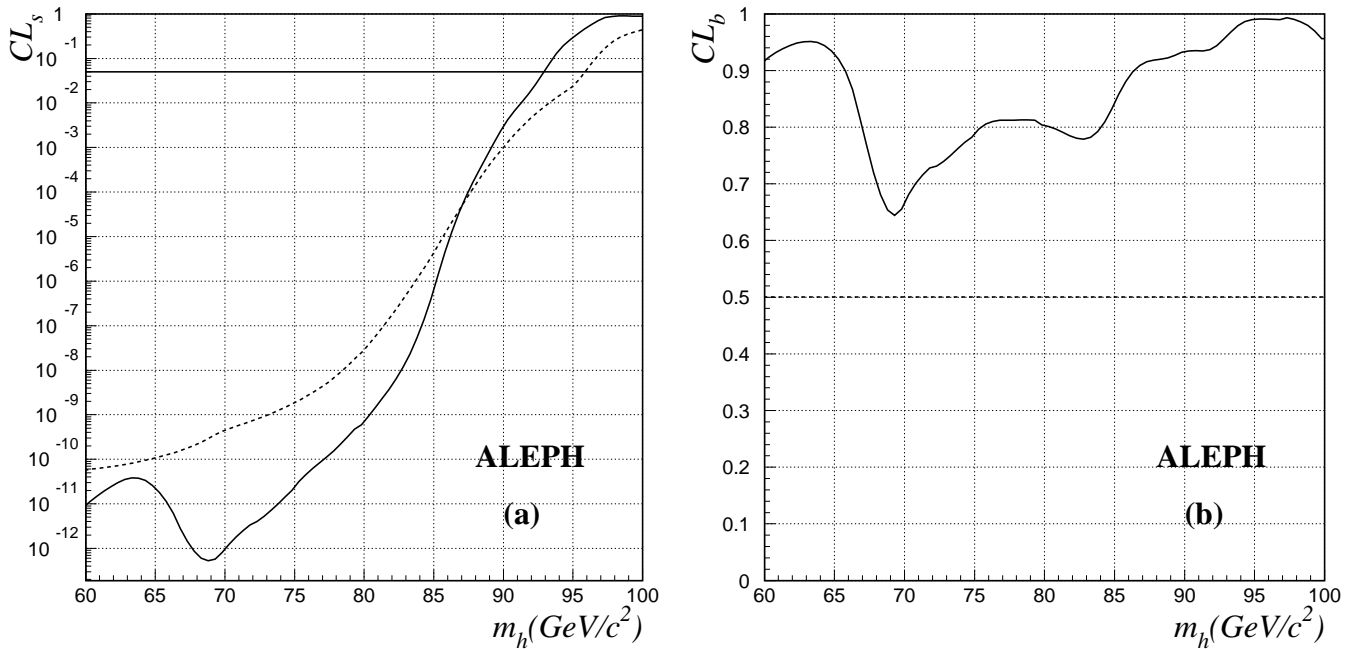|	h$\ell^+\ell^-$	h$\nu\bar{\nu}$				hq$\bar{q}$		h$\tau^+\tau^-$ / $\tau^+\tau^-$q$\bar{q}$
		NN(A)+NN(B)	NN(A)	NN(B)	Cuts	NN	Cuts	
n_s	1.5	2.0	0.3	0.7	2.6	8.5	7.3	0.7
n_b	14.0	3.1	0.7	2.4	7.3	21.4	19.0	2.5
n_{obs}	14	5	0	4	8	28	24	2

Fig. 7a,b. Expected (dashed) and observed (solid) CL curves, in the signal hypothesis **a** and in the background hypothesis **b**, as a function of the assumed Standard Model Higgs boson mass; the intersections of the horizontal line at 5% with the curves in **a** define the expected and observed 95% CL lower limits on the Higgs boson mass

Table 4. Expected signal, Standard Model background and observed candidate events in the statistically independent branches of the combined four-jet and b$\bar{b}\tau^+\tau^-$ analyses; $m_h = 95$ GeV/c^2 and $m_h = m_A = 85$ GeV/c^2 are assumed for the hZ and hA processes, respectively

Analysis		Expected events			Observed
		hZ	hA	SM background	candidates
	hZ only	6.6	1.0	18.8	24
hq$\bar{q}$	hZ+hA	1.9	2.8	2.6	4
	hA only	0.1	0.4	2.2	3
	hZ only	0.2	0.0	1.1	1
b$\bar{b}\tau^+\tau^-$	hZ+hA	0.4	0.4	1.4	1
	hA only	0.1	0.1	1.1	2

The result obtained with this method is displayed in Fig. 7 for the Standard Model Higgs boson. All Standard Model Higgs boson masses below 92.9 GeV/c^2 are excluded at the 95% CL. The average limit expected in the absence of signal is 95.9 GeV/c^2. With such an expected limit, the probability that an equal or lower limit be observed is 4%. (The observed and expected limits obtained with the cut-based combination of hZ analyses would be 93.9 GeV/c^2 and 95.4 GeV/c^2 respectively.) The procedure is repeated for the hZ process varying $\sin^2(\beta-\alpha)$, assuming branching ratios of the Standard Model Higgs boson. The resulting excluded domain is displayed in Fig. 9 (hZ curve).

The expected and observed CLs for the hA process are displayed in Fig. 8, for $m_h=m_A$ and $\sin^2(\beta-\alpha)=0$. With such assumptions, all Higgs boson masses below 82.5 GeV/c^2 are excluded at the 95% CL while the average limit expected in the absence of signal is 83.1 GeV/c^2. Varying $\sin^2(\beta-\alpha)$ while maintaining $m_h=m_A$ leads to the excluded domain shown in Fig. 9 (hA curve). Combining these results with those pertaining to the hZ channel, the combined exclusion shown in Fig. 9 is obtained. Inde-
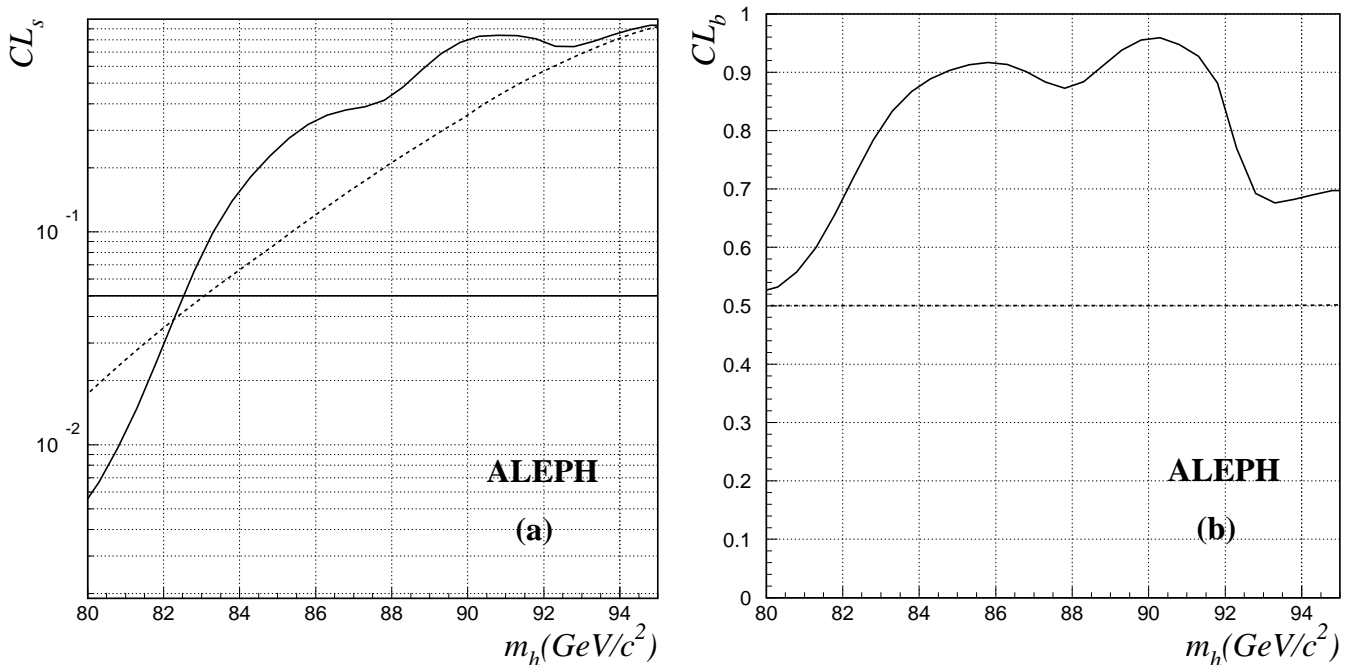
Fig. 8a,b. Expected (dashed) and observed (solid) CL curves for the hA pair-production process with $m_h = m_A$ and $\sin^2(\beta - \alpha) = 0$ as a function of the common mass, in the signal hypothesis **a** and in the background hypothesis **b**

pendent of $\sin^2(\beta - \alpha)$, all Higgs boson masses m_h below $82.5 \, \text{GeV}/c^2$ are excluded at more than 95% CL.

These results can also be interpreted in the $[m_h, \tan\beta]$ plane, as displayed in Fig. 10. Here, benchmark choices of the MSSM parameters are used, as suggested in [28]: the quadratic mean M_{SUSY} of the stop masses is set to $1 \, \text{TeV}/c^2$, the gaugino mass M_2 to $1.6 \, \text{TeV}/c^2$, the CP-odd Higgs boson mass is varied up to $400 \, \text{GeV}/c^2$, and two configurations of stop mixing are considered, with minimal and maximal impact on m_h; furthermore the top mass is fixed at $175 \, \text{GeV}/c^2$. If $\tan\beta$ is restricted to values greater than 0.7, an observed (expected) lower limit of 82.6 (83.2) GeV/c^2 is derived for m_A.

The combination of the experimental and theoretical exclusions shown in Fig. 10 excludes at 95% CL $\tan\beta$ values in the range [1.0,1.4], even when stop mixing has maximal impact. However, as emphasized in [29], such $\tan\beta$ exclusions are very sensitive both to the details of the calculations of the radiative corrections in the Higgs sector and to the choice of the top quark mass and MSSM parameter values. The above result is obtained using the calculations of [9] (*i.e.*, in the renormalization group improved one-loop effective potential approach), with a $175 \, \text{GeV}/c^2$ top mass; no exclusion range remains if a top mass of $180 \, \text{GeV}/c^2$ is used instead, or if additional genuine two-loop corrections are included as advocated in [30].

In the above CL computations, all systematic uncertainties have been included according to the prescription of [20]. Their effect results in decreasing the mass lower limits by 200 MeV/c^2. As explained in Sect. 6.1, the background level is known to be underestimated in the Monte Carlo due to b tag systematic uncertainties. The consequence of such an underestimation, when performing full

background subtraction, is a conservative observed limit and a slightly optimistic expected limit. This underestimation of the background does not fully explain the difference between observed and expected limits seen in Fig. 7. If, instead of using the method of [20], the reducible background levels had been decreased by one standard deviation, the mass lower limits would be decreased by no more than 400 MeV/c^2.

A more general hZ/hA combination is also performed in which the NN-based hZ analyses are combined with the cut-based analyses. The missing energy channel does not overlap with any hA analysis, but a combination of the two neural network analyses and the cut-based analysis is also performed. With three analyses, the most general division is into seven branches: three exclusives, three overlaps of two analyses and one overlap of three analyses. To reduce the complexity of the problem, some branches are joined together leaving in both cases only five branches. The information about these branches is summarised in Table 5. The expected limits obtained with these more general combinations are 83.1 GeV/c^2 and 95.8 GeV/c^2 at $\sin^2(\beta - \alpha) = 0$ and 1, respectively. Since the expected results are similar to those from the simplest combination, the latter is used to derive the final results.

8 Beyond the benchmark

It can be seen in Fig. 10 that low values of $\tan\beta$ are excluded by the present data in the benchmark scans for most configurations of stop mixing. In order to assess the robustness of this result with respect to variations of the
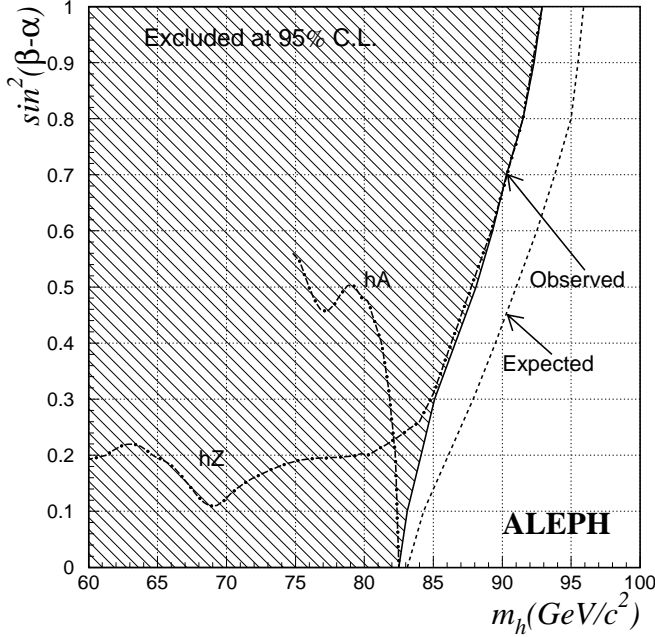
Fig. 9. Regions excluded at the 95% CL in the $[m_h, \sin^2(\beta-\alpha)]$ plane by the hZ and hA searches (dash-dotted curves) and their combination (solid curve). The dashed curve displays the expected 95% CL limit of the combination
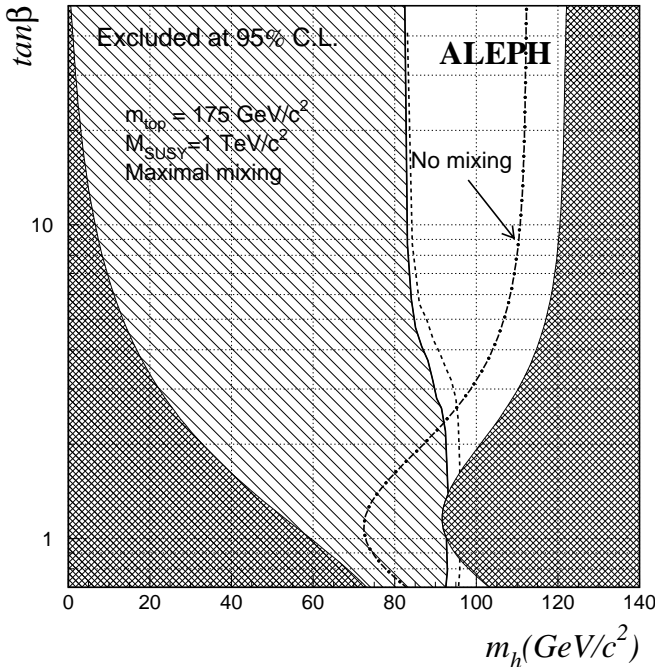
Table 5. Expected numbers of signal event (n_s), Standard Model background events (n_b) and observed data candidates (n_{obs}), in the statistically independent branches of the four-jet and missing energy channels. The signals are evaluated assuming $m_h = 95\,\mathrm{GeV}/c^2$ for hZ and $m_h = m_A = 85\,\mathrm{GeV}/c^2$ for hA

| | hq$\bar{q}$ | | | | |
	hA only	hA and hZ	NN	hZ only NN+Cuts	Cuts
n_s hZ	0.1	1.9	1.6	5.0	0.6
n_s hA	0.4	2.8	0.4	0.6	0.4
n_b	2.3	2.6	8.4	10.7	6.2
n_{obs}	3	4	9	15	4

| | h$\nu\bar{\nu}$ | | | | |
	Cuts only	Cuts and NN	NN only NN(A)	NN(A)+NN(B)	NN(B)
n_s	0.3	2.4	0.2	0.2	0.4
n_b	3.4	4.0	0.6	0.4	1.4
n_{obs}	1	7	0	1	1

Fig. 10. Expected (dashed) and observed (solid) 95% CL curves in the $[m_h, \tan\beta]$ plane of the MSSM in the case of maximal stop mixing; the dark regions are not allowed theoretically. The theoretically forbidden region is also indicated for the case of no stop mixing (dash-dotted curve)

MSSM parameters, an update of the parameter scan presented in [4] has been performed.

As in [4], the value $\tan\beta = \sqrt{2}$ is chosen as representative of the low $\tan\beta$ regime. In the "fine logarithmic" scan performed using the data collected up to 184 GeV, 352 869 sets of $\{m_0, m_{1/2}, \mu, A_t\}$ values were considered, the range explored extending up to 2 TeV/c^2 for m_0, $m_{1/2}$ and $|\mu|$, and up to 4 TeV/c^2 for $|A_t|$. For each of these sets, 35 values of m_A, logarithmically spaced up to 2 TeV/c^2, were tested, and the limit on m_h was obtained by dichotomy between the last excluded and first unexcluded m_A values. Additional dichotomies were performed, as detailed in [4], to explicitly search for "pathological" configurations, such as a vanishing hbb or hZZ coupling, which could invalidate the m_h limit thus determined. Among the $\{m_0, m_{1/2}, \mu, A_t\}$ sets examined, 36% were declared unphysical, due to tachyonic stops for example, and 52% were excluded irrespective of the value of m_A. The 41 352 (12%) remaining sets were not excluded for all values of m_A. For most of them, the m_h limit obtained in the benchmark scans held true. Only 28 (namely a fraction smaller than 10^{-4}) pathological sets remained with a mass limit significantly degraded because of either too small an hZ production cross section ($\sin^2(\beta-\alpha) \sim 0$), or of a vanishing branching ratio for h$\rightarrow$b$\bar{b}$ ($\sin\alpha \sim 0$). The 41 352 sets remaining unexcluded for some m_A values are reconsidered here in light of the improved Higgs limits reported in Sect. 7.

For the 41 324 parameter sets where the limit on m_h was found in [4] to be as high as in the benchmark scans, the hZ searches played the major rôle in the vicinity of the limit. With the updated exclusion in the $[m_h, \sin^2(\beta-\alpha)]$ plane (Fig. 9), 35 753 of these can now be excluded
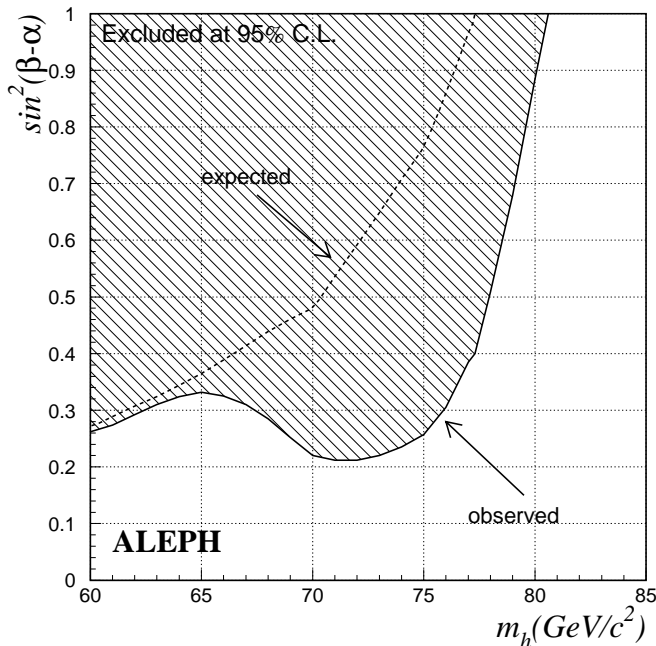
Fig. 11. Region in the $[m_{\rm h}, \sin^2(\beta - \alpha)]$ plane excluded at the 95% CL by the $h\nu\bar{\nu}$ search for a Higgs boson decaying into hadrons with no b tagging applied

irrespective of $m_{\rm A}$, while the limit obtained for the 5 571 other sets is essentially equal to the Standard Model one. No new pathological situations are encountered.

For most of the 28 pathological sets revealed in [4], the mass of the heavier CP-even Higgs boson H is relatively low, below 80 GeV/c^2, for the $m_{\rm A}$ value for which the $m_{\rm h}$ limit was set. The results from the hZ searches shown in Fig. 9 can therefore be used for HZ with the appropriate coupling modifications. This allows 22 sets to become excluded irrespective of the $m_{\rm A}$ value, leaving at this point six sets for which the mass limit is degraded.

For two of those sets (actually almost identical due to the approximate symmetry $A_{\rm t} \rightarrow - A_{\rm t}$, $\mu \rightarrow - \mu$), the limit on $m_{\rm h}$ is ~ 6.5 GeV/c^2 with $\sin^2(\beta - \alpha) \sim 0$. However, H is rather light (~ 73 GeV/c^2), but with a decay branching ratio into hh of 86%, rendering b tagging ineffective. The main h decay mode is h$\rightarrow\tau^+\tau^-$, with a branching ratio of 77%.

The process (H$\rightarrow$hh)(Z$\rightarrow\nu\bar{\nu}$) leads to a topology consisting of two low multiplicity acoplanar jets when h$\rightarrow \tau^+\tau^-$. A search for such final states has therefore been developed. The selection begins with the anti-$\gamma\gamma$ preselection of the 4J-L chargino analysis [31]. Only events with at most six charged tracks are considered. The events are divided into two hemispheres by a plane perpendicular to the thrust axis. Each hemisphere is required to contain two or four good charged tracks, and to have a mass smaller than 10 GeV/c^2. The efficiency of this search is 31% for $m_{\rm H} = 73$ GeV/c^2 and $m_{\rm h} = 6.5$ GeV/c^2, while the expected background is 0.3 events. No events are selected in the 189 GeV data. With the inclusion of this result in the scan, these two sets become excluded irrespective of the $m_{\rm A}$ value.

In the four remaining sets, the lower limit on $m_{\rm h}$ lies between 60 and 75 GeV/c^2, because of a too small branching fraction of h into b$\bar{\rm b}$. A search for h produced in association with a Z boson decaying into $\nu\bar{\nu}$ could be sensitive to these rather low $m_{\rm h}$ values, although no tagging of b hadrons can be used here to disentangle signal and background. An analysis has therefore been developed, along the lines of the three-neural-network analysis described in Sect. 5.2.4.

In this case, since no b tagging can be applied, the preselection is tightened: events with less than seven charged particles are rejected, and the minimum hemisphere energy is required to exceed $5\%\sqrt{s}$. Each of the two main backgrounds, q$\bar{\rm q}$ and WW, is addressed by a dedicated neural network trained on a 75 GeV/c^2 mass signal. Cuts on both NN outputs are determined using the same optimisation procedure as for all the searches reported above. Finally, the cut $E_{12} < 3.5\%\sqrt{s}$ is applied. The signal efficiency is 50%, while the background level is estimated to be 14.3 events. Twelve candidate events are selected in the 189 GeV data.

This search, based on the h$\nu\bar{\nu}$ process only, results in the upper limit on $\sin^2(\beta - \alpha)$ as a function of $m_{\rm h}$ shown in Fig. 11. This limit is valid in the case of a Higgs boson decaying into any hadrons. When added to the other constraints, the result of this search is sufficient to exclude the four remaining pathological sets, irrespective of $m_{\rm A}$.

In the end, no configurations of parameters could be found, for $\tan \beta = \sqrt{2}$, for which the Higgs boson mass limit is significantly degraded with respect to the benchmark scans. To obtain this result, over twelve million sets of $\{m_0, m_{1/2}, \mu, A_{\rm t}, m_{\rm A}\}$ values were considered, and, in addition, a systematic search for pathological configurations was performed along the $m_{\rm A}$ direction for each $\{m_0, m_{1/2}, \mu, A_{\rm t}\}$ set. Finally, an exploration of the parameter space along the other directions was made in the vicinity of some typical pathological sets thus identified, which did not reveal any configurations leading to a degraded limit. In the low $\tan \beta$ regime of the MSSM, the limit from the benchmark scans can therefore be regarded as robust.

The above conclusion is affected neither by the choice of the top quark mass nor by the inclusion of recently calculated higher order radiative corrections [30]. Such modifications do not introduce any new pathologies, and simply change the relative proportions of parameter sets excluded irrespective of $m_{\rm A}$ and of sets for which the $m_{\rm h}$ limit is essentially the Standard Model one. A similar statement can be made regarding the results which will be obtained at higher LEP energies, in the event of no discovery.

9 Conclusions

Searches for neutral Higgs bosons in e$^+$e$^-$ collisions at a centre-of-mass energy of 188.6 GeV have been carried out with the ALEPH detector. The major event topologies expected from the hZ and hA processes have been analysed. The previously published search algorithms have been improved and complemented with new event selections. In

the collected data sample, which corresponds to an integrated luminosity of $176.2\,\mathrm{pb}^{-1}$, the selected events are compatible with expectations from Standard Model processes. From this observation, a 95% CL lower limit on the mass of the Standard Model Higgs boson is set at $92.9\,\mathrm{GeV}/c^2$. In the MSSM, lower limits of $82.5\,\mathrm{GeV}/c^2$ and $82.6\,\mathrm{GeV}/c^2$ are derived for the masses of the neutral Higgs bosons h and A, respectively, for all values of $\tan\beta \geq 0.7$. Other collaborations at LEP have reported similar results [32]. The robustness of these results in the low $\tan\beta$ regime has been assessed by a scan of the MSSM parameter space.

References

1. ALEPH Collaboration, Search for the Standard Model Higgs boson in e^+e^- collisions at $\sqrt{s} = 161$, 170 and 172 GeV, Phys. Lett.**B412**(1997) 155
2. ALEPH Collaboration, Search for the Standard Model Higgs Boson at the LEP2 collider near $\sqrt{s} = 183$ GeV, Phys. Lett.**B447**(1999) 336
3. ALEPH Collaboration, Search for the neutral Higgs bosons of the MSSM in e^+e^- collisions at $\sqrt{s}$ from 130 to 172 GeV, Phys. Lett.**B412**(1997) 173
4. ALEPH Collaboration, Searches for the Neutral Higgs Bosons of the MSSM in e^+e^- collisions at centre-of-mass energies of 181-184 GeV, Phys. Lett.**B440**(1998) 419
5. ALEPH Collaboration, ALEPH: A detector for electron-positron annihilations at LEP, Nucl. Instrum. Methods **A294**(1990) 121
6. ALEPH Collaboration, Performance of the ALEPH detector at LEP, Nucl. Instrum. Methods **A360**(1995) 481
7. D. Creanza et al., The New ALEPH Vertex Detector, Nucl. Instrum. Methods **A409**(1998) 157
8. P. Janot, The HZHA generator, in "Physics at LEP", Eds. G. Altarelli, T. Sjöstrand and F. Zwirner, CERN 96-01 (1996) Vol. 2, p. 309
9. M. Carena, M. Quiros and C. Wagner, Effective potential methods and the Higgs mass spectrum in the MSSM, Nucl. Phys.**B461**(1996) 405
10. S. Jadach, Z. Wąs, R. Decker and J.H. Kühn, The τ decay library TAUOLA, version 2.4, Comput. Phys. Commun.**76**(1993) 361
11. T. Sjöstrand, High-energy-physics event generation with PYTHIA 5.7 and JETSET 7.4, Comput. Phys. Commun.**82**(1994) 74
12. S. Jadach, B.F.L. Ward and Z. Wąs, The Monte Carlo program KORALZ version 4.0 for the lepton or quark pair production at LEP/SLC energies, Comput. Phys. Commun.**79**(1994) 503
13. M. Skrzypek et al., Monte Carlo program KORALW 1.02 for W-pair production at LEP2/NLC energies with Yennie-Frautschi-Suura exponentiation, Comput. Phys. Commun.**94**(1996) 216
14. This generator is based on the differential cross section published in S. Ambrosanio and B. Mele, Anomalous WWZ couplings at future e^+e^- colliders, Nucl. Phys.**B374**(1992) 3
15. W.T. Eadie et al., Statistical Methods in Experimental Physics, North-Holland Publishing Company, 1971
16. DELPHI Collaboration, Search for neutral Higgs bosons in e^+e^- collisions at $\sqrt{s} = 183$ GeV, submitted to E. Phys. J. C
17. H. Hu and J. Nielsen, Analytic Confidence Level Calculations using Likelihood Ratio and Fourier Transform, `physics/9806010`, to be published in High Energy Phys. and Nucl. Phys. (English edition)
18. P. Janot and F. Le Diberder, Optimally combined confidence limits, Nucl. Instrum. Methods **A411**(1998) 449
19. S. Jin and P. McNamara, The Signal Estimator Limit Setting Method, `hep-ph/9812030`, submitted to Nucl. Instrum. Methods A
20. R.D. Cousins and V.L. Highland, Incorporating systematic uncertainties into an upper limit, Nucl. Instrum. Methods **A320**(1992) 331
21. W. Kilian, M. Kramer and P.M. Zerwas, Higgsstrahlung and W W fusion in e^+e^- collisions, Phys. Lett.**B373**(1996) 135; Higgsstrahlung and vector boson fusion in e^+e^- collisions, `hep-ph/9605437`
22. W. J. Stirling, Hard QCD Working Group—Theory Summary, J. Phys. **G17** (1991) 1567
23. ALEPH Collaboration, Measurement of hadron and lepton-pair production from e^+e^- annihilation at centre-of-mass energies of 130 and 136 GeV, Phys. Lett.**B378**(1996) 373
24. ALEPH Collaboration, Measurement of W-pair production in e^+e^- collisions at 189 GeV, ALEPH 99/017 CONF 99/012, contributed paper to HEP-99, Tampere, #6_045
25. ALEPH Collaboration, A precise measurement of $\Gamma_{Z\rightarrow b\bar{b}}/\Gamma_{Z\rightarrow hadrons}$, Phys. Lett.**B313**(1993) 535
26. ALEPH Collaboration, Search for an invisibly decaying Higgs boson in e^+e^- collisions at 189 GeV, Phys. Lett.**B466**(1999) 50
27. ALEPH Collaboration, A measurement of the gluon splitting rate to $b\bar{b}$ pairs in hadronic Z decays, Phys. Lett.**B434**(1998) 437
28. M. Carena, P.M. Zerwas (Convenors), Higgs Physics, in Physics at LEP2, Eds. G. Altarelli, T. Sjöstrand, F. Zwirner, CERN 96-01 (1996) p. 351
29. S. Heinemeyer, W. Hollik and G. Weiglein, Constrains on $\tan\beta$ in the MSSM from the Upper Bound on the Mass of the Lightest Higgs Boson, DESY 99-120, KA-TP-12-1999 and `hep-ph/9909540`
30. M. Carena, S. Heinemeyer, C.E.M. Wagner and G. Weiglein, Suggestions for Improved Benchmark Scenarios for Higgs-Boson Searches at LEP2, CERN-TH/99-134, DESY 99-186 and `hep-ph/9912223`
31. ALEPH Collaboration, Search for Charginos and Neutralinos in e^+e^- Collisions at Centre-of-Mass Energies near 183 GeV and Constraints on the MSSM Parameter Space, CERN-EP/99-014, to be published in Eur. Phys. J. C
32. L3 Collaboration, Search for the Standard Model Higgs boson in e^+e^- interactions at $\sqrt{s} = 189$ GeV, CERN-EP/99-080, submitted to Phys. Lett. B. OPAL Collaboration, Search for Neutral Higgs Bosons in e^+e^- Collisions at $\sqrt{s} \approx 189$ GeV, CERN-EP/99-096, submitted to Eur. Phys. J. C